

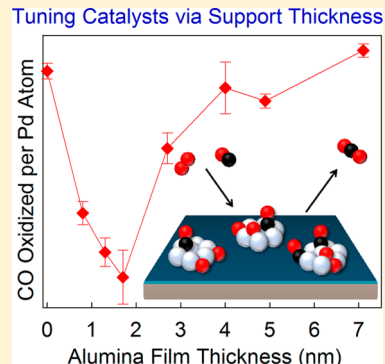
Effects of Alumina Thickness on CO Oxidation Activity over Pd₂₀/Alumina/Re(0001): Correlated Effects of Alumina Electronic Properties and Pd₂₀ Geometry on Activity

Matthew D. Kane, F. Sloan Roberts, and Scott L. Anderson*

Department of Chemistry, The University of Utah, 315 S. 1400 E, Salt Lake City, Utah 84112, United States

Supporting Information

ABSTRACT: The CO oxidation activity of size-selected Pd₂₀ clusters deposited on alumina films grown on Re(0001) is shown to depend strongly on the film thickness in the 0 to 10 nm range. For the reaction conditions of these experiments, binding and activation of O₂ is shown to be the limiting process, which can be varied by a factor of 2 by tuning the alumina film thickness, due to effects on both the electronic structure of the alumina film and the morphology of the supported Pd clusters. The alumina films are shown to be doped with Re atoms diffusing from the Re(0001) substrate, leading to a strong dependence of the surface electronic properties on alumina thickness, which in turn, results in the observed thickness-dependent activity of the Pd₂₀.



1. INTRODUCTION

Ultrathin oxide films grown on metal single crystals are frequently used as supports for metal-on-metal oxide model catalysts, allowing the full array of surface analysis tools to be used in mechanistic studies, without complications from surface charging that can limit use of bulk oxide supports.^{1–28} One obvious question is how thick the oxide layer must be to realistically represent a bulk oxide, and for thinner oxide films, what effects on chemistry might result. The oxide thickness can influence the geometry of supported metal nanoparticles,^{12,29} and the electronic properties of the oxides can be thickness dependent,^{30,31} which, as shown below, also influences the electronic properties of supported particles. Tunneling of electrons from the metal support to metal particles through a thin oxide layer can also occur.^{3,32} In addition, the presence of impurity atoms in the oxide arising from the underlying substrate can influence binding and electronic properties of metal particles supported on the oxide.³³ Calorimetry has shown that metal oxide adsorption energies vary significantly for oxide support films thinner than ~2 nm.³⁴ Theory has also been used to examine thickness effects, focusing on electron transfer, work function changes, and defects.^{12,32,35–37}

Here, we use CO oxidation over Pd₂₀ clusters deposited on variable thickness alumina films to probe thickness effects. One commonly used alumina film model is the self-limiting alumina film that grows spontaneously on NiAl single crystals heated in O₂. For example, on NiAl(110), a 0.5 nm thick film grows which has excellent order, as shown by both STM and X-ray crystallography.^{26,38–42} The Freund group has used this model system in a number of studies, including CO oxidation over Pd nanoparticles supported on alumina/NiAl(110). Such films are

initially too thin to block diffusion of oxygen activated on the Pd to the NiAl substrate, but under oxidizing conditions, the alumina film gradually thickens enough to be a good catalyst support.⁴³ For our very small Pd_n clusters, this approach was unsuccessful,⁴⁴ and the experiments here were made using alumina films grown using evaporative procedures developed by the Madey^{30,31} and Goodman^{45,46} groups, who demonstrated ordered films on Ta(110) and Re(0001) supports. CO oxidation was chosen as the test reaction because there is a wealth of mechanistic information about this reaction catalyzed by both single crystals^{47–50} and oxide-supported metal particles.^{1,9,48,51–57} CO oxidation occurs by a Langmuir–Hinshelwood mechanism, where CO and oxygen coadsorb and then react at metal sites.^{49,50,58,59} Vajda and co-workers reported a study of the thermal stability of Pt clusters deposited on alumina films grown on oxidized silicon substrates, demonstrating that the Pt clusters were stable at elevated temperatures on complete films.⁶⁰ Similarly, Pd_n clusters deposited on alumina films grown Ta(110) were also shown to be stable in terms of exposed Pd surface area and CO oxidation reactivity for at least eight reaction cycles reaching temperatures of 600 K.⁶¹

Here, we report a study of the effects of varying alumina film thickness on the CO oxidation activity of deposited Pd₂₀ clusters. In addition, we examine the electronic properties of both the alumina films and the deposited clusters, as well as the cluster morphology and the density of different types of binding

Received: September 15, 2014

Revised: December 17, 2014

Published: December 18, 2014

sites, all as a function of alumina film thickness. We previously reported a study of cluster size effects on CO oxidation over $\text{Pd}_n/\text{alumina}/\text{Re}$,⁶² and Pd_{20} was chosen as having chemistry and electronic properties representative of clusters in the 7 to 30 atom size range. Our interest here is partly in exploring ways that oxide thickness might be used to tune catalytic properties, but mostly we focus on using thickness-dependent correlations of activity with various physical properties to learn about the reaction mechanism. One of the advantages of cluster deposition is that it is possible to deposit clusters of a particular size (Pd_{20}), independent of coverage and of the density of defects on the oxide support. For a system like ultrathin alumina on Re(0001), the number, type, and density of defects almost certainly vary with thickness. As a result, samples grown by nucleation of evaporated Pd atoms would tend to have particle size distributions that vary with alumina thickness.

It is observed that CO oxidation activity is strongly dependent on the thickness of the alumina support, with a minimum in the range between one and two nanometers. A number of properties of the alumina films and the supported clusters are shown to have correlated dependence on thickness, and a model is developed which accounts for both the dip in activity, and the accompanying changes in the properties of the alumina and the supported Pd_{20} . In essence, the free electron density in the alumina film, due to Re impurities, results in thickness-dependent electron transfer to Pd_{20} that affects both its electronic properties and binding morphology, in ways that cause a drop in activity.

2. EXPERIMENTAL METHODS

The methodology has been described previously,^{62–64} and additional details can be found in the Supporting Information. Samples were prepared by depositing Pd_{20}^+ on alumina thin films grown on a $10 \times 5 \times 1$ mm Re(0001) single crystal (Marketech International Inc.). Alumina films with thicknesses up to at least 7 nm are conductive enough that the Pd_{20}^+ neutralize upon deposition with no signs of charging, and by integrating the neutralization current, deposition could be stopped with Pd coverage totaling 1.53×10^{14} Pd atoms/cm², equivalent to 0.1 of a close-packed Pd monolayer. Deposition was carried out at room temperature with typical deposition times of about 5 min.

The alumina film growth procedure was adapted from the Goodman and Madey groups.^{30,31,46} The Re(0001) crystal was cleaned by annealing at 1775 K for 20 min, until no contaminants could be detected via XPS. After cleaning, the sample was lowered into the antechamber and heated to 970 K, while Al was vapor deposited in a background of 5×10^{-6} Torr of ultrahigh purity $^{16}\text{O}_2$ that was further cleaned by passing it through a liquid nitrogen/ethanol bath (~160 K). The Al/Re XPS intensity ratio was used to estimate the thickness of the alumina film, using literature values for the photoemission cross sections and β parameters⁶⁵ and effective attenuation lengths calculated from the NIST EAL Database version 1.3.⁶⁶ We estimate that the absolute thicknesses are correct to within ~20%; however, the relative uncertainty in comparing thicknesses of different films is estimated to be less than 5%.

The as-prepared $\text{Pt}_{20}/\text{alumina}/\text{Re}$ samples were characterized by X-ray photoelectron spectroscopy (XPS) at room temperature, measuring the Re 4f, O 1s, Al 2s, and Pd 3d binding energies. Immediately after XPS characterization, the sample cryostat was cooled, and then the samples were flashed to 560 K to desorb any adventitious adsorbates. As-prepared

samples were also examined using ultraviolet photoelectron spectroscopy (UPS) and low energy He^+ ion scattering (ISS); however, these experiments required separately prepared sets of samples, to avoid any possibility that ion impact damage (ISS) or adventitious adsorbates (UPS) might interfere with reactivity studies. Because sample preparation is quite time-consuming, UPS and ISS experiments were done only for selected samples.

CO oxidation was studied using temperature-programmed reaction (TPR) experiments, which consisted of first dosing the $\text{Pd}_{20}/\text{alumina}/\text{Re}$ samples with 10 L of $^{18}\text{O}_2$ at 400 K, followed by a 10 L dose of ^{13}CO at 180 K. The 180 K CO dose temperature was chosen as being high enough to avoid CO sticking to the alumina support film but low enough to minimize reaction of impinging CO with the previously dosed $^{18}\text{O}_2$. A short pulse of $^{13}\text{C}^{16}\text{O}^{18}\text{O}$ was observed at the beginning of the ^{13}CO dose; however, this amounted to only ~2–3% of the total $^{13}\text{C}^{16}\text{O}^{18}\text{O}$ produced during the TPR experiments, and at least some of this $^{13}\text{C}^{16}\text{O}^{18}\text{O}$ is attributable to ^{13}CO reacting with ^{18}O left on the inner surface of the CO dose tube during the $^{18}\text{O}_2$ exposure. We have, therefore, omitted this small $^{13}\text{C}^{16}\text{O}^{18}\text{O}$ signal from the integrated desorption estimates. After the O_2 and CO exposures, samples were cooled to 135 K, moved to a position 1 mm from the orifice of a skimmer cone isolating the UHV chamber from a differentially pumped mass spectrometer. The samples were heated at 3 K/s while desorption signal was measured by both the differentially pumped mass spectrometer and a second mass spectrometer monitoring changes in the UHV chamber background. The masses monitored included all isotopologues of CO and CO_2 , as well as water; however, the only significant desorption signals were masses 29 (^{13}CO) and 47 ($^{13}\text{C}^{16}\text{O}^{18}\text{O}$). The absence of other CO or CO_2 isotopologues indicates that ^{16}O from the alumina film was not involved in the chemistry and that any adventitious ^{12}CO that may have bound to the surface was desorbed during the 560 K flash or reacted away during the 400 K oxidation step. After the initial TPR measurement, two additional TPR measurements (with 400 K $^{18}\text{O}_2$ and 180 K ^{13}CO exposures) were made in quick succession, in order to examine TPR-induced changes in the model catalyst properties. Finally, the reactivity sequence was ended with a CO temperature-programmed desorption (CO-TPD) experiment to probe the density and type of CO binding sites present. For CO-TPD, the sample was exposed only to 10 L of ^{13}CO at 180 K, cooled to 135 K, and heated at 3 K/s while monitoring the same masses as in the TPR runs. Only ^{13}CO desorption was significant.

The mass spectrometer sensitivity to desorbing CO and CO_2 was calibrated by measuring signal intensities for known densities of both gases, checked daily. Absolute CO and CO_2 desorption amounts derived from this calibration are estimated to be within a factor of 2 of the correct values, as described elsewhere.⁶² Because both CO and CO_2 originate from Pd sites, and we know the number of Pd atoms deposited (as Pd_{20}) quite precisely, we report the desorption signals as CO or CO_2 molecules desorbing per Pd atom.

3. RESULTS

ISS Characterization of the As-Prepared Pd/Alumina/Re Samples. Figure 1a shows raw ISS spectra for various freshly prepared samples. The figure shows results for films up to 4.6 nm thick because the spectra are visually similar for thicker films. ISS results for samples after the sequence of three

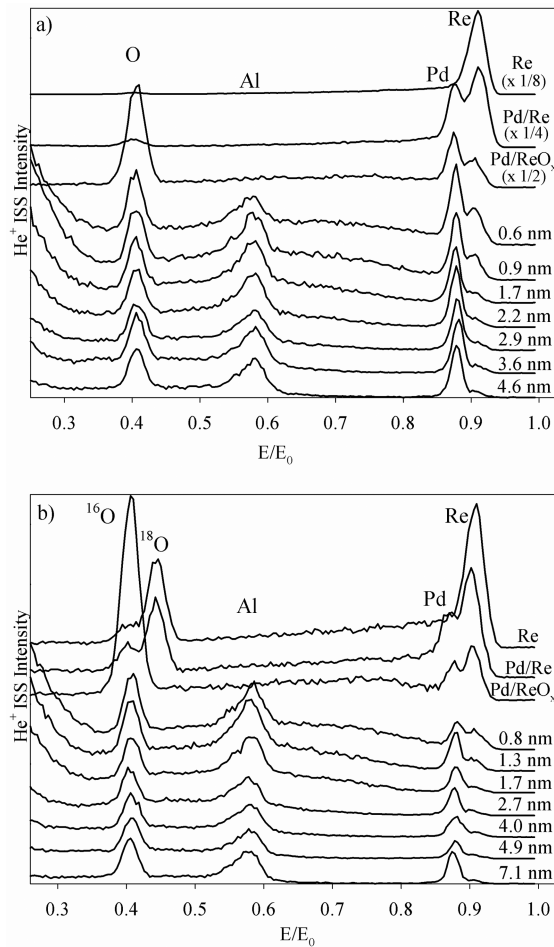


Figure 1. He^+ ISS for $\text{Re}(0001)$, 0.1 ML Pd_{20} on $\text{Re}(0001)$, and 0.1 ML Pd_{20} on alumina films of increasing thicknesses. (a) Freshly deposited samples. (b) Post reaction. Note scale factors for the first three spectra in frame a. Peaks centered at 0.40, 0.44, 0.57, 0.88, and 0.92 correspond to ^{16}O , ^{18}O , Al, Pd, and Re.

TPR and one TPD experiments are shown in Figure 1b and will be discussed below. Consider the as-prepared results in Figure 1a. The top spectrum is for the freshly cleaned $\text{Re}(0001)$ substrate, showing a large peak for He^+ scattering from Re, as well as barely noticeable signal in the E/E_0 range expected for ^{16}O , reflecting the presence of a small amount of surface oxygen. Because the next step in sample preparation was oxidation with $^{16}\text{O}_2$, no attempt was made to eliminate this small ^{16}O impurity. Note that this spectrum has been scaled by a factor of 0.125, because He^+ scattering from Re is quite intense.

The rest of the spectra are for samples with 0.1 ML Pd_{20} deposited. The “Pd/Re” spectrum has Pd_{20} deposited directly on freshly annealed, unoxidized $\text{Re}(0001)$ and is scaled by a factor of 0.25. For this spectrum peaks are observed both for Pd and for Re, and the weak signal for ^{16}O is more apparent due to the larger scale factor.

The more important spectra are for Pd_{20} deposited on oxidized samples with variable thickness alumina films. The “Pd/ ReO_x ” spectrum is for Pd_{20} deposited on Re that was oxidized under the same conditions used for alumina film growth, but without aluminum evaporation (note 0.5 scaling). As expected, this spectrum shows a large peak for ^{16}O , a peak for Pd, and a peak for Re which is substantially attenuated by

the presence of ^{16}O (and Pd_{20}) in the surface layer. The rest of the spectra are for Pd_{20} deposited on various thickness alumina films grown on oxidized $\text{Re}(0001)$. Each has peaks for ^{16}O and Al and for Pd and Re. As expected for a series of samples containing identical Pd_{20} coverage, the Pd ISS intensity is roughly constant; however, there are subtle variations, discussed below, that indicate thickness-dependent changes in sample morphology.

The Al peak intensity is essentially constant except for the films with thickness ≤ 0.9 nm, where the Al intensity decreases. Given that ISS peak intensities are primarily sensitive to atoms in the surface layer, this pattern suggests that the alumina films are discontinuous for thicknesses ≤ 0.9 nm but are continuous for films thicker than ~ 1.7 nm. This conclusion is consistent with reports from the Madey³⁰ and Goodman^{45,46} groups who found that their films became continuous at about 1.5 nm thickness.

Even for the thickest films, there is still a weak ISS signal in the E/E_0 range expected for Re. We previously showed that growth of a 0.5 nm thick alumina film on $\text{NiAl}(110)$ was sufficient to completely attenuate the Ni ISS signal from the NiAl substrate.⁶⁷ Therefore, to explain the weak Re signal remaining well past the thickness where the films are continuous, we propose that Re diffuses into the alumina film at the high growth temperature, resulting in Re surface concentrations that decrease with increasing film thickness. This situation is similar to that recently reported for CaO films grown on Mo supports.³³ The surface layer Re concentration can be estimated by comparing the Re ISS intensity for each sample with that measured for unoxidized $\text{Re}(0001)$, where the surface density is known. As summarized in Figure S1 of the Supporting Information, the Re concentration is estimated to be $\sim 0.5\%$ for 10 nm alumina films, increasing slowly with decreasing film thickness to $\sim 2.2\%$ for the 1.7 nm film. For the 0.9 and 0.6 nm films, there is a sharp increase in the Re surface concentration, reaching $\sim 9\%$ for the 0.6 nm film; however, this is in the range where both the literature^{30,31,46} and our Al ISS intensities suggest that the alumina film is no longer continuous. The sharp increase for the thinnest films is attributed to the appearance of exposed ReO_x patches between alumina islands which make up $>90\%$ of the surface.

Given the conclusion that there are patches of exposed ReO_x for the thinnest alumina films, it is useful to know the level of Re oxidation under different O_2 exposures. The “Pd/ ReO_x ” spectrum in Figure 1a shows that exposure of $\text{Re}(0001)$ to alumina growth conditions ($\sim 6000 \text{ L } \text{O}_2$ at 970 K) results in a large ($\sim 3:1$) $\text{O}:\text{Re}$ ISS intensity ratio, implying that the surface is heavily oxidized. Since all the alumina/Re samples received the $\sim 6000 \text{ L}$, 970 K O_2 exposure during the alumina growth, any exposed ReO_x should be heavily oxidized. Exposure of unoxidized $\text{Re}(0001)$ to the 10 L, 400 K $^{18}\text{O}_2$ exposure used in TPR also oxidizes the surface, but not as thoroughly. Figure 1b (spectrum “Re”) has an $(^{16}\text{O}+^{18}\text{O}):\text{Re}$ ratio of just 1:1.15.

TPR Studies of Reactivity. The CO oxidation activity of the samples was studied by a sequence of TPR experiments, followed by a final CO TPD experiment. The only significant desorption signals during TPR were for unreacted ^{13}CO and the expected $^{13}\text{C}^{16}\text{O}^{18}\text{O}$ product. The TPR process (O_2 and CO exposures, 3 K/s heating) was repeated twice to probe the stability of the samples under heating and adsorbate exposure, and then a final CO TPD run was done (only CO exposure, 3 K/s heating). The $^{13}\text{C}^{16}\text{O}^{18}\text{O}$ desorption in the first of the TPR measurements for select samples is shown in Figure 2a, and

Figure 2b summarizes the integrated $^{13}\text{C}^{16}\text{O}^{18}\text{O}$ production in the three TPR runs as a function of alumina film thickness.

The top trace in Figure 2a shows that the alumina films are inert under these conditions. The second spectrum shows another control experiment, demonstrating that there was also no CO oxidation catalyzed by the Re(0001) support. As discussed above, the $^{18}\text{O}_2$ exposure used in TPR results in significant oxidation of the Re(0001) surface, but this oxygen is evidently too strongly bound to react with CO, which also adsorbs on this sample (see below).

When Pd_{20} was deposited directly on unoxidized Re(0001), there was substantial $^{13}\text{C}^{16}\text{O}^{18}\text{O}$ production during the first TPR run (Figure 2a, “Pd/Re”), amounting to ~ 0.25 molecules per Pd atom on the surface. In subsequent TPR runs on this sample, the $^{13}\text{C}^{16}\text{O}^{18}\text{O}$ signal decreased by $\sim 50\%$ per run (solid points in Figure 2b for zero film thickness). The postreaction ISS in Figure 1b shows that, for the “Pd/Re” sample, the Pd

intensity was significantly lower after reaction compared to the as-prepared sample; i.e., the fraction of Pd in the surface layer was decreased. Since the TPRs only involved heating to 550 K, evaporation of the Pd is unlikely; therefore, both the loss of CO oxidation activity and of Pd ISS intensity are attributed to changes in Pd morphology, which could include processes such as sintering or Pd dissolution into the Re bulk. We note that when Pd_n was deposited on an unoxidized Ta(110) surface at room temperature, ISS showed no Pd in the surface layer, demonstrating that diffusion into the bulk can be rapid, even for refractory metals at modest temperatures.⁶¹

As noted above, the thinnest alumina films are thought to be discontinuous, exposing small patches of ReO_x . To probe the chemistry of Pd_{20} on such oxidized Re areas, Figure 2a shows $^{13}\text{C}^{16}\text{O}^{18}\text{O}$ production from Pd_{20} deposited on ReO_x prepared by exposing Re(0001) to ~ 6000 L O_2 at 970 K. This “Pd/ ReO_x ” sample has integrated $^{13}\text{C}^{16}\text{O}^{18}\text{O}$ production activity of ~ 0.26 CO_2/Pd atom, all of which can be attributed to activity of the supported Pd_{20} , since the oxidized Re is inert. The CO_2 signal from $\text{Pd}_{20}/\text{ReO}_x$ is quite stable from run to run, as shown by the open points at zero thickness in Figure 1b. Evidently, the heavily oxidized ReO_x surface provides a stable support, possibly because the oxide layer is thick enough to block diffusion into the bulk.

The rest of Figure 2a shows data for a selection of samples prepared by depositing 0.1 ML Pd_{20} on various thickness alumina films grown on Re(0001). It can be seen that the $\text{Pd}_{20}/$ alumina samples are all active for $^{13}\text{C}^{16}\text{O}^{18}\text{O}$ production, and that even for the thinnest films, the temperature dependence for $^{13}\text{C}^{16}\text{O}^{18}\text{O}$ desorption is quite different from those for $\text{Pd}_{20}/$ Re or $\text{Pd}_{20}/\text{ReO}_x$. For all Pd/alumina samples, $^{13}\text{C}^{16}\text{O}^{18}\text{O}$ desorption occurs in a broad, essentially structureless feature, starting at 180 K, peaking near 300 K, and extending to just over 500 K. CO_2 was not observed to stick to $\text{Pd}_{20}/$ alumina/Re at 180 K, suggesting that the temperature dependence of the TPR signal reflects the kinetics of $^{13}\text{C}^{16}\text{O}^{18}\text{O}$ formation from adsorbed ^{13}CO and ^{18}O (or $^{18}\text{O}_2$), rather than the energetics for desorption of the CO_2 product. It is interesting that all the $\text{Pd}_{20}/$ alumina/Re samples give such similar temperature dependences, despite the indication from ISS that there is significant ReO_x exposed in the 0.8 nm alumina film (Figure S1, Supporting Information).

In Figure 2b it can be seen that the activity is reasonably stable from run to run, increasing slightly in successive TPR runs for samples with ≤ 4 nm alumina films. One of the interesting features shown in Figure 2b is that the CO oxidation activity initially decreases sharply with increasing alumina thickness, passing through a minimum for films around 2 nm, and then increases to a thickness-independent level for films thicker than ~ 4 nm. Understanding the mechanistic origins of this modulation of activity in the 1–4 nm thickness range is one of the main goals of this study.

Desorption of CO provides a different probe of the samples' chemical properties. Figure 3a shows the desorption of residual, unreacted ^{13}CO during the first TPR run on each sample, and Figure 3b shows ^{13}CO desorption during the final CO TPD experiment run after the three TPRs. As with the CO_2 desorption data, we show only a selection of the results for the $\text{Pd}_{20}/$ alumina/Re samples.

For alumina grown on Re(0001), no CO desorption is observed in either the TPR or TPD experiments, indicating that CO does not stick on the alumina support. In both TPR and TPD on Pd-free Re(0001), ^{13}CO desorbs in a strong feature

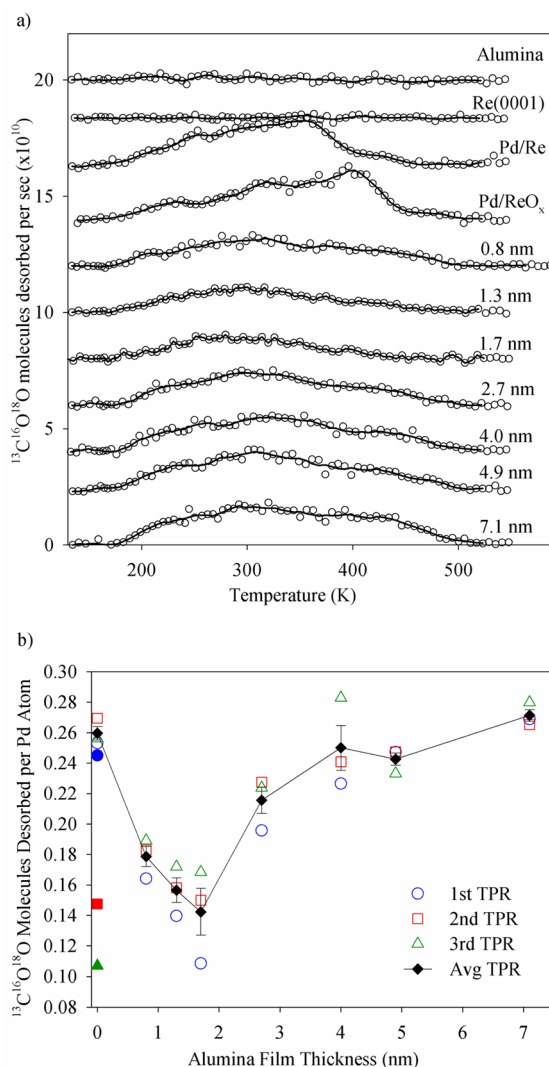


Figure 2. (a) $^{13}\text{C}^{16}\text{O}^{18}\text{O}$ signal temperature dependence measured in the first TPR cycle on the indicated samples (see text for explanation). (b) Integrated $^{13}\text{C}^{16}\text{O}^{18}\text{O}$ signals measured during three consecutive TPR runs, along with the average from the three runs. The solid points at zero alumina thickness are for Pd_{20} deposited on unoxidized Re(0001), and the open points are for Pd_{20} deposited on oxidized Re(0001).

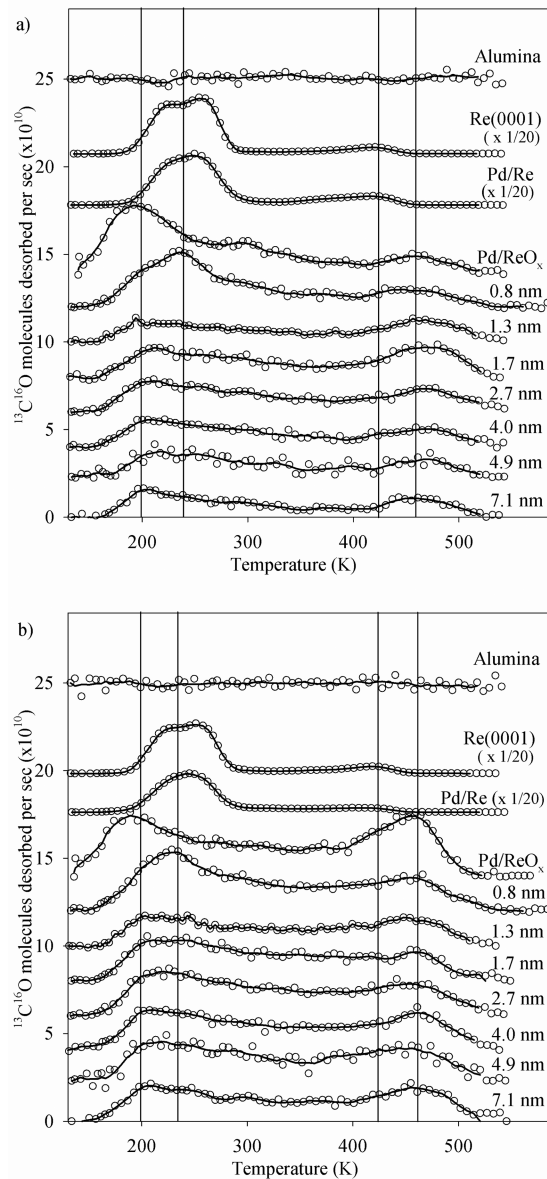


Figure 3. (a) Desorption temperature dependence for unreacted CO in the first TPR run on each of the indicated samples. (b) Desorption temperature dependence for CO in a final CO TPD run on each sample, made after the set of three TPR runs.

between 180 and 280 K, presumably corresponding to CO on terrace sites (note $\times 0.05$ scaling). Note that under these conditions, the Re surface was lightly oxidized; however, no CO_2 production was observed. There is also a weak feature in both TPR and TPD near 425 K, attributed to CO bound to defects. Deposition of 0.1 ML of Pd_{20} on the Re surface prior to oxidation has little effect on CO desorption, presumably because the Pd coverage is low and CO sticks efficiently to the lightly oxidized Re surface.

For Pd_{20} deposited on heavily oxidized Re (“Pd/ReO_x”), the total amount of unreacted CO desorbing during TPR is much lower than for the lightly oxidized samples, peaking just above the 180 K CO dose temperature, with a long tail connecting to weak desorption features peaking near 300 and 460 K. The weak intensity and the observation that the main peak occurs just above the dose temperature suggest that that desorption temperature for CO bound to ReO_x terraces is below the 180 K

dose temperature and that we are only observing CO desorbing from Pd_{20} and from defect sites on the ReO_x support. The fact that CO binding to ReO_x is weak and that CO does not stick at all to alumina/ReO_x is useful from the perspective allowing CO desorption from Pd_{20} to be observed clearly. For this Pd/ReO_x sample, a significant fraction of the adsorbed CO was oxidized to CO_2 in the TPR runs (Figure 1). In the final TPD, where no CO_2 production occurred, there was a significant increase in CO desorption near 460 K, suggesting that CO in these more strongly bound sites was the predominant contributor to the CO_2 production.

The Pd_{20} /alumina/Re samples show residual CO desorption during TPR (Figure 2a) in two broad components, peaking at ~ 200 K and at ~ 460 K. The integrated amount of unreacted CO desorbing during TPR is weakly dependent on alumina thickness, ranging from ~ 0.26 CO/Pd atom (5.2 CO/Pd₂₀) for samples in the 1.5 to 3 nm range, decreasing to ~ 0.22 CO/Pd atom (4.4 CO/Pd₂₀) for the thicker films. CO desorption from $\text{Pd}_n/\text{TiO}_2(110)$ and $\text{Pd}_n/\text{alumina/Ta}(110)$ is also bimodal, and in those systems we used temperature-dependent ISS to probe the nature of the CO binding sites, with the result that the low temperature binding feature was found to be primarily associated with CO bound at the periphery of the clusters, while the high temperature feature was primarily associated with CO desorbing from sites on top of the clusters.^{62,64,68} ISS probes binding geometry by observing attenuation of scattering from the Pd clusters due to CO binding in different sites, and details of the binding geometries are unknown. Thus, “on top” could include any sites where CO would attenuate ISS from the underlying Pd, and we cannot distinguish between atop, bridging, or hollow site binding.

For the sample with alumina thickness of 0.8 nm, the desorption behavior is slightly different, as might be expected since the thinnest films are thought to be discontinuous,^{30,45,46} exposing some ReO_x. Surprisingly, the temperature dependence is not what might be expected for Pd_{20} on alumina with a small fraction of Pd_{20} on ReO_x, the latter of which might be expected to result in a lowered onset temperature for CO desorption. Instead, the low temperature CO desorption feature appears to have “extra” intensity around 230 K, and as a result, the integrated CO desorption increases to ~ 0.31 CO/Pd atom, compared to 0.26 to 0.22 CO/Pd for the thicker films. It is not clear where this extra CO is binding, but discontinuous films may provide CO binding sites at alumina–ReO_x boundaries or on Pd_{20} deposited at such boundaries. In addition, we will show that the electronic properties of both the alumina and the deposited Pd_{20} are strongly dependent on alumina thickness, which may lead to additional CO binding. Whatever the origin, the absence of this 230 K feature for all the samples with films thicker than ~ 1.3 nm is further evidence that the thick alumina films are continuous.

If we assume that oxidation and desorption are the only two channels consuming adsorbed CO during TPR, then the sum of the desorption signals for CO_2 and CO provides an estimate for the total amount of CO adsorbed under TPR conditions, i.e., with preadsorbed oxygen. Total CO is found to be roughly constant at ~ 0.48 CO/Pd atom for samples with alumina films of ≥ 3 nm thickness, corresponding to ~ 10 CO molecules adsorbed per Pd_{20} cluster. Because the $\sim 50\%$ dip in CO_2 production for alumina films in the 0.8 to 2 nm thickness range (i.e., 10 CO/Pd₂₀) is partially offset by an increase in desorption of residual CO, the total CO adsorption only drops to ~ 0.4 CO/Pd (8 CO/Pd₂₀). The ratio of integrated

intensities $\text{CO}_2/(\text{CO}+\text{CO}_2)$ is essentially the efficiency with which adsorbed CO is converted to CO_2 , and it ranges from ~34% in the 0.8 to 2 nm range to ~52% for Pd_{20} on thick alumina films. Finally, from the amount of CO_2 produced, we can estimate lower limits on amount of active oxygen bound to the samples after the 400 K 10 L O_2 exposure, which vary from 3 to 5 O atoms per Pd_{20} , depending on film thickness. The fact that no O_2 desorption is ever seen, no CO_2 is observed in the final CO TPD, and no ^{18}O is left on the surface (see below) suggests that the actual amount of adsorbed oxygen is close to these lower limits.

In the final TPD measured after the series of TPR runs, the CO desorption observed for the $\text{Pd}_{20}/\text{alumina}/\text{Re}$ samples (Figure 3b) is qualitatively similar to that observed in the first TPR, with broadly bimodal desorption and similar peak temperatures. The main difference is that in the final CO TPD, the integrated amount of CO desorbing is ~70% higher, approximately independent of alumina film thickness. An increase is not surprising and is attributable to two factors. In TPR, 34–52% of the initially adsorbed CO is converted to CO_2 , but this competing channel is absent in TPD. In addition, we might expect that the O_2 exposure used in TPR might block CO adsorption sites, further reducing the amount of residual CO desorption.

As noted, one of the main goals of this study is to explore the factors that cause the ~50% dip in CO oxidation activity for alumina films with thicknesses between ~0.8 and 3 nm. One obvious potential correlation is between activity and CO desorption, since both depend on the number and energetics of binding sites on the samples. To separate the low and high temperature desorption components, each TPR and TPD spectrum was fit, as shown in Figure S2 of the Supporting Information. We looked for various correlations, and the two that emerged are shown in Figure 4. Activity is found to be inversely correlated with the integrated intensity of the high temperature component of residual (unreacted) CO desorbing during TPR (note inverted scale). Such an anticorrelation is not

surprising, because CO oxidation is in competition with desorption of residual CO. The more interesting observation is that there is a strong positive correlation of activity with the high temperature component of CO desorbing in the final TPD. The implications of this correlation will be discussed below.

ISS Studies of Adsorbate Binding and the Effects of the Reaction Sequence. ISS can also be used to probe the nature of adsorbate binding to samples and is sensitive to both the number and the binding geometries. Here, ISS was used to probe oxygen and CO binding, although only a few such experiments were done because each required preparation of several fresh samples to avoid ISS damage effects. Typical ISS data for as-deposited $\text{Pd}_{20}/\text{alumina}/\text{Re}$ (Figure 1a) have peaks for O, Al, Pd, and a small shoulder for Re in the alumina film. The 10 L, 400 K O_2 exposure used in TPR was found to cause no change in O, Al, or Re intensities, but oxidation did result in a 15–20% attenuation of the Pd intensity. This can be contrasted to a ~70–80% attenuation of Pd signal by the 10 L 180 K CO exposure used in TPR. As discussed above, we estimate that the average number of active O atoms per Pd_{20} ranged from 3 to 5, while the total adsorbed CO was ~10 CO/ Pd_{20} .

Adsorbate attenuation of ISS signals results from three effects.^{69,70} Adsorbates bound on top of the surface prevent He^+ scattering from surface layer atoms that lie within shadow cones cast by the adsorbate atoms. In our geometry, these shadow cones are cast at 45° with respect to the surface normal. Another attenuation process is blocking, where He^+ scatters from a Pd atom but then is prevented from reaching the detector because the adsorbate atom lies in between. Since we detect along the surface normal, blocking occurs if adsorbates are bound in atop sites. Finally, when He^+ trajectories pass through the electron cloud of adsorbates, neutralization can occur, reducing the ion survival probability (ISP) and thus ISS signal. All three mechanisms will tend to attenuate the Pd ISS signal for adsorbates bound on top of the Pd_{20} clusters, but cause little effect for adsorbates binding to the surrounding alumina support or in sites at the cluster periphery.

The 15 to 20% Pd ISS attenuation observed from adsorption of 3 to 5 O atoms per Pd_{20} implies that each O atom attenuates signal from roughly one Pd atom. This strong attenuation is consistent with oxygen binding on top of the clusters but does not allow us to distinguish between atop, bridge, or hollow sites. The larger attenuation from CO exposure reflects the higher (10 CO/Pd_{20}) coverage but also the fact that CO has two atoms, each casting shadow cones and having an electron cloud that decreases ISP. As noted above, if CO exposure is done without preadsorbed O, ~70% more CO sticks, and the Pd ISS remains strongly attenuated. In fact, temperature-dependent ISS experiments on $\text{Pd}_n/\text{TiO}_2(110)^{64}$ and $\text{Pd}_n/\text{alumina/Ta}(110)^{62}$, which show bimodal CO desorption profiles similar to those in Figure 3, suggest that only CO desorbing in the high temperature component is bound on top of the clusters, and the low temperature CO desorption occurs from peripheral sites.

Several interesting features are also observed in the postreaction ISS characterization (Figure 1b). Note that for the Re and Pd/Re samples, new peaks are observed corresponding to ^{18}O on the surface, resulting from oxidation of the Re by the 10 L, 400 K $^{18}\text{O}_2$ exposure. In contrast, no ^{18}O signal is observed for Pd/ReO_x or for any of the $\text{Pd}/\text{alumina}/\text{Re}$ samples, indicating that both the alumina and ReO_x films are

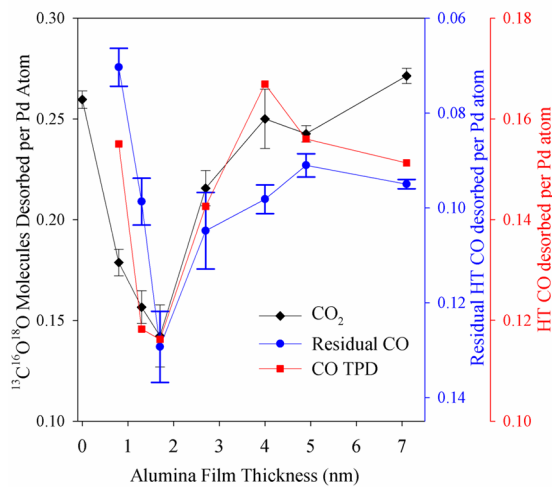


Figure 4. Black: Integrated CO_2 production averaged over the three TPR measurements on each sample, as a function of alumina film thickness. Blue: Integrated desorption of unreacted CO from the high temperature binding site, averaged over the three TPR runs (note inverted scale). Red: CO desorbing from the high temperature binding site in the final CO TPD run, after the set of TPR runs.

stable with respect to oxygen exchange, and that there is no significant spillover of unreacted ^{18}O from the Pd clusters to the oxide supports. The Pd ISS intensities in the postreaction samples are all somewhat smaller than in the analogous as-prepared samples, showing that the fraction of Pd in the surface layer was reduced. Such decreases can result from reaction-induced sintering of the clusters; however, in this case they simply result from accumulation of adventitious adsorbates on the Pd, because ISS was done after XPS, during which time (20 min) the samples were at ~ 120 K. Supported cluster samples are highly efficient at binding adsorbates via a substrate-mediated process where molecules (e.g., CO) initially bind (weakly) to the alumina support but diffuse to stable binding sites on the Pd clusters.^{62,64,71} The presence of such adsorbates can be verified, and corrected for, by analysis of Pd ISS intensity vs exposure to the He^+ beam, which preferentially sputters adsorbates.^{64,70} We did this analysis for $\text{Pd}_n/\text{alumina}/\text{Re}$ as part of a study of cluster size effects, and after correction for adsorbates, the Pd signals before and after reaction were found to be identical.⁶²

Sample Electronic Properties as a Function of Alumina Thickness. The electronic structure of the as-prepared alumina films and films with supported Pd_{20} were characterized using a combination of UPS and XPS. The raw UPS for a selection of samples are shown in Figure 5a with the binding energy (BE) scale referenced to the Fermi level (E_F) of the Re(0001) support. The spectra are broken into three segments, plotted with different intensity scaling in order to show the important features more clearly. The region near E_F is plotted with $4.5\times$ magnification of the intensity scale, to allow the weak signals to be observed more clearly. The region between 4 and 8 eV shows the onset and peak of the alumina valence ("O 2p") band, which dominates the spectra. In this energy range, the energy axis has been expanded slightly to allow the small shifts to be observed more clearly. The region between 8 and 14 eV is omitted because it simply shows a slow decline of the alumina valence band. Finally, the region above 14 eV is plotted on a $100\times$ expanded intensity scale, with the energy scale also expanded to allow shifts in the high BE spectral limits to be observed more clearly. The high BE spectral limits can be used to calculate the sample work functions: $\Phi = h\nu - \text{BE}_{\text{limit}}$, where Φ is the sample work function, $h\nu$ is the photon energy (21.21 eV), and BE_{limit} is the high BE spectral limit. The work function results are summarized in Figure 5b.

The spectrum for freshly cleaned Re(0001) has a sharp onset at E_F , little signal in the O 2p region, and $\text{BE}_{\text{limit}} \approx 15.47$ eV, implying $\Phi \approx 5.72$ eV. This measured Φ is ~ 0.75 eV higher than literature value reported⁷² for Re(0001), and we attribute the difference to the presence of a small amount of surface oxygen on the as-prepared Re(0001) (Figure 1a). For the oxidized Re support ("Re O_x "), there is still a sharp onset at E_F , with additional structure both in the near- E_F and O 2p regions, reflecting Re–O binding. BE_{limit} decreases to 13.85 eV, corresponding to an oxidation-induced increase in Φ to ~ 7.35 eV.

For alumina/Re samples, the spectra change systematically with alumina thickness. In the near- E_F region, the signal from the underlying Re substrate decreases rapidly with increasing film thickness, because Re photoelectrons are attenuated during passage through the alumina film. For the thicker films, there is little intensity remaining in the alumina band gap region, between E_F and ~ 4.5 eV. As expected, the alumina valence (O

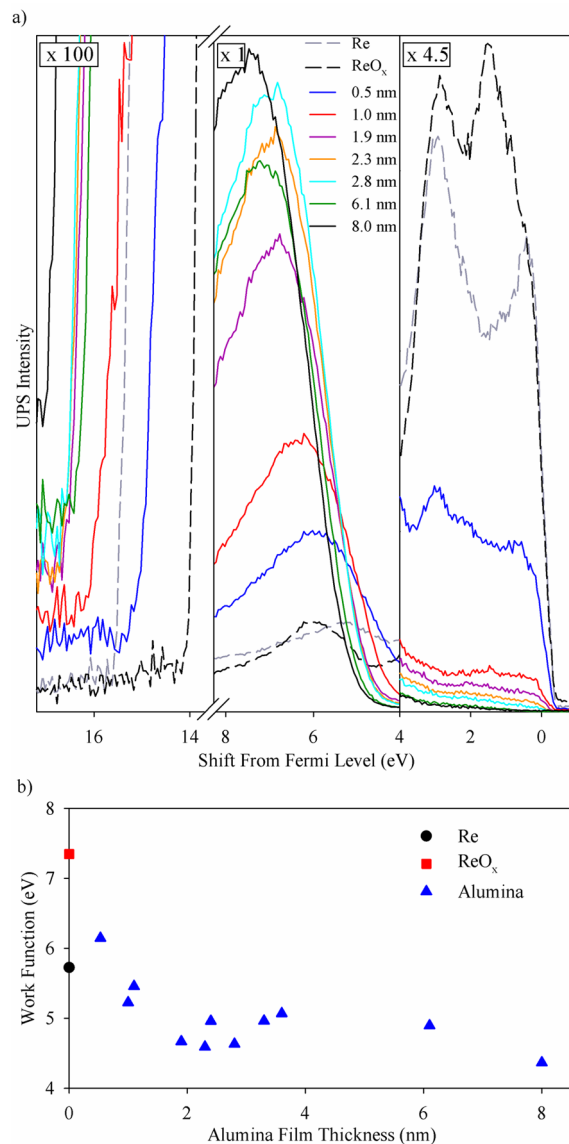


Figure 5. (a) UPS spectra taken for Re(0001) with various thicknesses of alumina films. The spectra have been broken into three energy ranges in order to show features of interest more clearly by applying different scale factors. Spectra are shown for clean Re(0001), Re(0001) after oxidation, and oxidized Re(0001) with alumina overlayers of the indicated thicknesses. (b) Work functions determined from the high energy cutoff of each spectrum.

2p) band intensity increases with thickness and then becomes nearly thickness-independent for films thicker than ~ 3 nm. There are also slight shifts in the onset and peak energies of this feature. With increasing alumina thickness, BE_{limit} also increases, implying a gradual decrease in the sample work function from ~ 6 eV for the thinnest films to 4.37 eV for the 8 nm film.

The UPS and XPS results for the alumina valence and core levels of the as-prepared samples are summarized in Figure 6a, and results are given for samples with and without Pd_{20} deposited. Because the alumina valence band is quite broad, what is plotted is actually the valence band onset energy, i.e., the BE at the top of the valence band, which was estimated using a method suggested by Parkinson and Schlaf et al.^{73,74} The rising edge of the band was fit to a Gaussian-convoluted

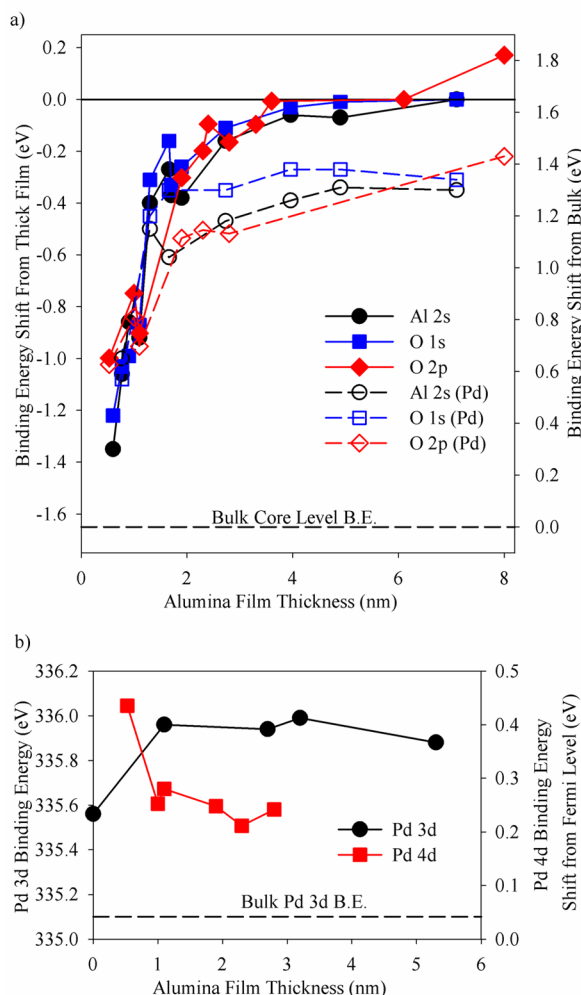


Figure 6. (a) Shifts in binding energies for the Al 2s and O 1s core orbitals as well as the O 2p valence level as a function of alumina film thickness. The left scale shows the shift relative to binding energies measured for the thickest film where no charging occurred. The right scale shows shifts relative to bulk alumina. (b) The Pd 3d core level binding energy and the top of the Pd 4d valence band as a function of alumina thickness, relative to the sample Fermi level.

step function, and then the slope at the inflection point was extrapolated to baseline to estimate the onset energy. To allow all the results to be plotted together, the figure plots *shifts* in the BEs, and scales are provided for shifts relative to both literature BEs for bulk alumina and to the limiting BEs measured here for thick alumina films. For both core and valence BEs, the “thick film limit” was taken as the thickest film where there was no evidence of charging during photoemission. Because different sets of samples were used in the XPS and UPS work, this was the 7.1 nm film for XPS data and a 6.1 nm film for UPS. The increase in BEs for the 8 nm film is a sign that charging is significant for such thick films. Note that the BEs *do not converge* on the bulk limit with increasing alumina thickness. Instead, they reach a nearly constant value that is shifted ~1.65 eV above the bulk limit. The shifts are slightly different for the O 1s and Al 2p levels (1.7 and 1.6 eV, respectively).

The valence and core levels of the alumina films show remarkably similar shifts with changing alumina thickness. For

films thicker than ~3 nm, the BEs are essentially thickness-independent and shifted by 1.65 eV with respect to bulk alumina. For thinner films, the BEs decrease but remain well above the bulk alumina limit, even for the thinnest films. Deposition of 0.1 ML of Pd₂₀ reduces both the core and valence BEs associated with the thicker alumina films by ~0.4 eV but has little effect on the alumina BEs for films thinner than ~1.2 nm.

In addition to measuring the electronic properties of the alumina support film, we also used UPS and XPS to characterize both valence and core levels of the deposited Pd₂₀ as a function of the alumina thickness. An example comparing raw UP spectra for alumina/Re and Pd₂₀/alumina/Re is shown in Figure S3 of the Supporting Information. The alumina in this example was 2.8 nm thick, and only a weak and featureless signal was observed in the alumina band gap, between E_F and the top of the alumina valence band at ~4.5 eV. Upon Pd₂₀ deposition, the signal was clearly seen in the band gap region, and the ~0.4 eV deposition-induced shift in the onset of the alumina valence band is also noticeable. The Pd signal was analyzed by subtracting out the spectrum measured for the alumina/Re substrate (inset), and then the onset of the Pd band was extracted using the same fitting/extrapolation method used to analyze the alumina valence band.

The Pd 3d core level BEs and onset energies of the Pd valence band are summarized in Figure 6b. For Pd₂₀ deposited directly on either Re(0001) or on ReO_x, the Pd 3d BE is ~335.5 eV, i.e., essentially identical to that for bulk Pd. For Pd₂₀ deposited on alumina/Re, the binding energies are shifted to ~336.0, with no obvious trend with varying film thickness. These measurements have relatively large uncertainty (~±0.2 eV) due to low Pd signal from 0.1 ML coverage and background from inelastic scattering of 4d photoelectrons from the Re support. The observation that the BEs for Pd₂₀/alumina are greater than that for bulk Pd could be taken as evidence for electron transfer from Pd to alumina; however, as discussed below, we believe that the Pd actually accepts electrons from alumina and that the positive BE shifts reflect reduced final state screening for small clusters supported on an insulating layer.^{75–79}

For films thicker than ~1 nm, the onset of the Pd valence band is 0.25 ± 0.04 eV below E_F , i.e., the Pd₂₀/alumina samples still have a band gap, essentially independent of alumina film thickness. The onset energy for the sample with Pd₂₀ deposited on a 0.5 nm alumina film is apparently shifted ~0.2 eV to higher binding energy; however, for such a thin film there is still substantial intensity in the band gap region from the Re substrate (Figure 5a), resulting in high uncertainty for the subtraction/fitting analysis used to extract the Pd valence band onset. Within the uncertainty, therefore, neither the core nor valence levels shift significantly with alumina thickness, even though the alumina levels, themselves, shift by more than 1 eV.

The observed changes in alumina BEs with thickness (Figure 6a) are signatures of thickness-dependent variations in sample electronic properties and are not simply artifacts of sample charging under the VUV or X-ray beams. If beam-induced charging were significant in this thickness range, then the core and valence BEs of the Pd₂₀ deposited on the films should show shifts similar to those of the alumina support, rather than being essentially thickness-independent (Figure 6b). Furthermore, the alumina XPS peak widths should tend to increase with thickness due to differential charging, whereas widths actually decrease. Only for films thicker than ~8 nm do we begin to see

obvious signs of beam-induced charging (increasing BE shifts and peak broadening).

BEs were also measured after O₂ exposure. The BEs associated with the alumina film did not change, but the inset to Figure 7 compares the Pd 3d BEs for as-deposited samples, with those measured after a 10 L ¹⁸O₂ exposure identical to that in the first step of the TPR experiments. As expected for an oxidation reaction, the Pd BEs shift to higher energy, but the amount of the shift is dependent on the alumina thickness. As shown in the main frame of Figure 7, the thickness dependence of this oxidation-induced core level shift appears to be correlated with the CO oxidation activity. We have only two data points for oxidation-induced shifts in the onset energy of the Pd valence band, but the valence band shifts also appear to correlate with activity.

Correlation between Pd ISS Intensity and Activity.

Figure 8 shows another correlation of activity with a physical property of the samples. As mentioned above, there is a weak dependence of the as-deposited Pd ISS intensity on the thickness of the alumina film on which Pd₂₀ is deposited. As Figure 8 shows, the Pd ISS intensity has dependence on thickness that correlates well with the thickness-dependent CO oxidation activity. Note that the as-deposited Pd ISS intensities in this figure are not simply the ISS peak intensities from Figure 1a, although the thickness dependence there is quite similar. The intensities have been corrected for the effects of any adventitious adsorbates that might have bound to Pd during deposition, using a process discussed elsewhere,^{64,71} in which the Pd intensity is monitored as a function of He⁺ flux and extrapolated back to the limit of zero exposure and zero adsorbate coverage.

Since all the samples have the same Pd coverage, the Pd ISS intensities are essentially a measure of the fraction of the Pd in the surface layer; i.e., they are sensitive to the cluster

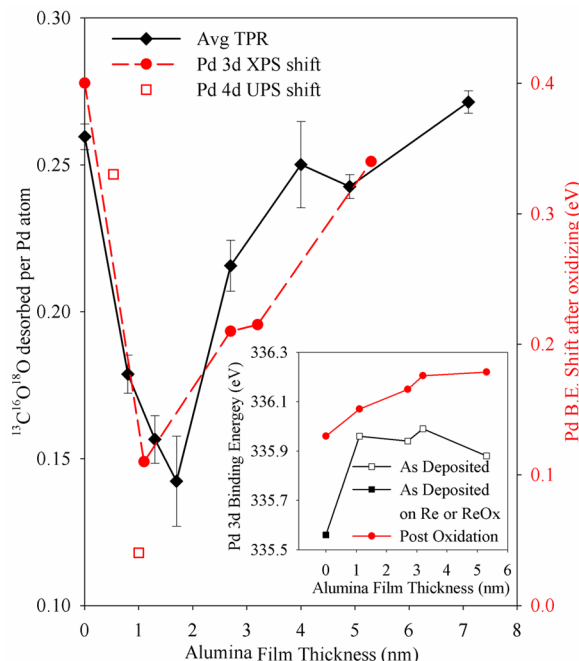


Figure 7. Inset: Raw Pd 3d binding energies for as-deposited Pd₂₀ and after exposure to 10 L ¹⁸O₂ at 400 K. Main figure: The shift in Pd 3d and 4d binding energies from O₂ exposure are compared to the CO oxidation activity over a range of alumina thicknesses.

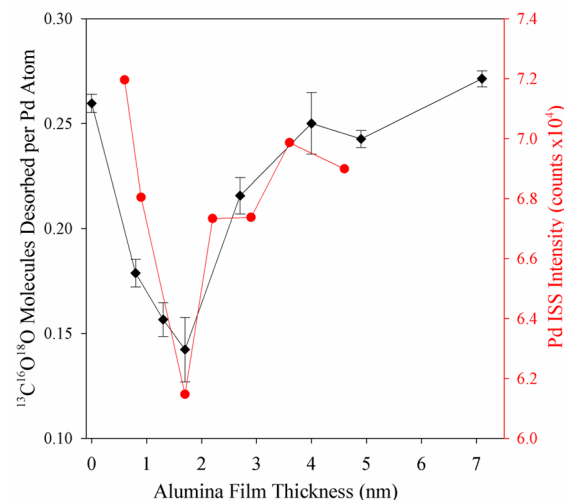


Figure 8. Comparison of CO₂ production activity (black—left axis) and Pd ISS intensity (red—right axis) as a function of alumina thickness.

geometries. It is not surprising that a smaller number of Pd surface sites would be correlated with lower activity; however, the ISS intensity only dips by ~14% at the minimum, compared to a ~50% reduction in activity. Clearly the decrease in activity is not simply a Pd surface area effect, although it may be a contributing factor.

4. DISCUSSION

At this point, we have shown correlations of activity with Pd ISS intensity, with the density of particular CO binding sites, and with the shift in Pd BEs upon O₂ exposure. Correlation does not imply causation, and in the discussion below we attempt to show how these observations are interrelated and what they tell us about the factors responsible for the thickness-dependent activity.

Rate Limiting Factors under TPR Conditions and Thickness Correlations. The interpretation of the activity correlations depends on the reaction mechanism, i.e., the rate-limiting factors under our TPR conditions. Fortunately, CO oxidation over Pd single crystals^{47,49,50,58,80,81} and various supported Pd nanoparticle samples^{82–86} have been well studied, and there is considerable mechanistic information available. The factors limiting activity are strongly dependent on reaction conditions. For example, CO sticks efficiently and binds stably to Pd over a broad temperature range, while O₂ sticking and activation are less efficient, although binding is strong.^{9,87–89} When CO and O₂ are both present, the two reactants compete for Pd binding sites.^{49,50,58} Therefore, at low temperatures the Pd sites tend to rapidly become poisoned by CO, and the absence of adsorbed oxygen limits CO₂ production. Under steady-state reaction conditions, Pd catalysts are typically not active until the temperature is raised to the point where the CO lifetime on the Pd sites becomes short enough to leave sites available for O₂ adsorption. The TPR protocol used here was done with both O₂ and CO exposures at relatively low temperatures (to minimize thermal effects on the clusters), but the O₂ exposure was done first, precisely to avoid CO poisoning. For sufficiently large O₂ exposures, oxygen coverage can become large enough to block sites needed for CO adsorption, thereby reducing activity,⁸⁸ and the 10 L exposure used here was chosen to avoid this issue as well. The 10 L CO

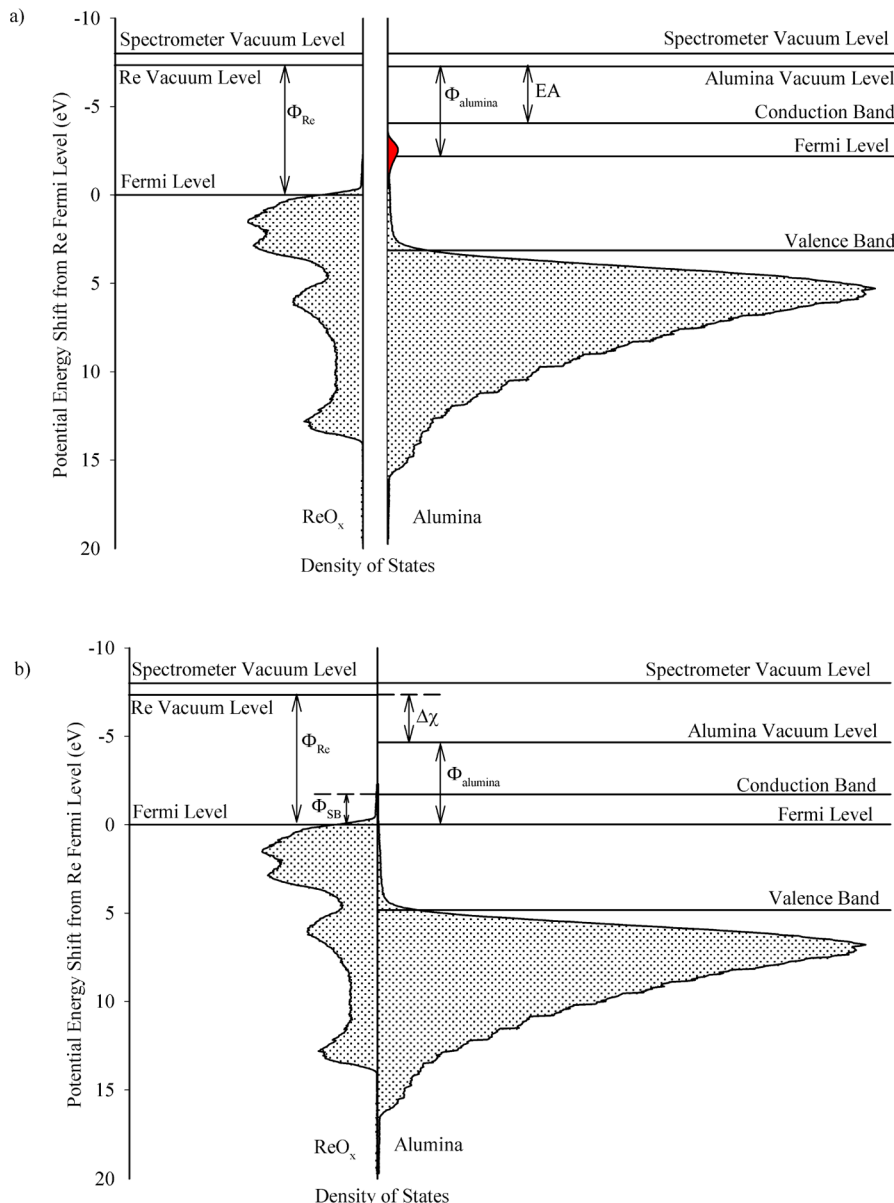


Figure 9. Diagram illustrating the density of states for ReO_x and Re-doped alumina based on measured UPS. (a) Situation before ReO_x and alumina are brought into contact. (b) Situation after contact. The red DOS shown for the alumina film in (a) is an exaggerated estimate of the population of states near the conduction band due to Re dopants.

exposure is sufficient to saturate any Pd sites left unoccupied after the oxygen exposure, and the 180 K CO exposure temperature is low enough that reaction impinging CO with the preadsorbed oxygen is negligible, as discussed above.

For the more active catalysts (i.e., Pd_{20} on either ReO_x or on thick alumina films), comparison of the desorption signals for CO_2 and unreacted CO shows that only $\sim 50\%$ of the adsorbed CO reacts, the rest desorbing unreacted. In addition, the fact that no CO_2 production is seen in the final TPD, either during the CO exposure or subsequent heat ramp, indicates that there is no active oxygen left on the surface at the end of the preceding TPR run. Finally, the absence of any ^{18}O signal in the postreaction ISS shows that none of the $^{18}\text{O}_2$ used in the TPR is left in the surface layer after the reaction sequence. Taken together, these data show that there is surplus CO on the surface and that the active adsorbed oxygen is completely

consumed during TPR, i.e., that active oxygen is the activity-limiting reactant.

Figure 4 shows that activity is positively correlated with the intensity of CO desorbing in the high temperature feature in CO TPD, and an analogous positive correlation (varying cluster size rather than alumina thickness) was seen for $\text{Pt}_n/\text{alumina}/\text{Re}$ catalysts under similar conditions.⁹⁰ For both Pd and Pt, activity appears to be limited primarily by the amount of oxygen activated on the clusters by the O_2 dose, and the obvious interpretation of the correlation is that O_2 activation occurs on the same sites that are responsible for the strongest CO binding, so that samples with the largest number of such sites are the most active and also have the strongest CO desorption features. Temperature-dependent ISS shows that these sites are predominantly on top of the clusters, in both cases.^{62,64} It is interesting, therefore, that there is an anticorrelation between activity and this high temperature

feature measured for residual CO desorbing during TPR. The anticorrelation presumably stems from competition between CO desorption and CO oxidation. Samples which have large numbers of “on top of cluster” sites suitable for O₂ activation (or CO binding in TPD) have more oxygen bound after the O₂ exposure, bind less CO in these sites, and convert more of the CO to CO₂.

In a number of previous studies of cluster size effects on oxidation catalytic activity,^{61,62,71,91} we have found size-dependent anticorrelations between core and valence level BEs of the metal clusters, and activity as oxidation catalysts under conditions ranging from UHV to aqueous phase electrochemistry. As shown in Figure 7, the situation here is different. The Pd core and valence level BEs for Pd₂₀/alumina/Re samples are essentially independent of the alumina thickness, despite the observation that both core and valence levels of the alumina film are strongly thickness dependent. Instead, CO oxidation activity is correlated with shifts in both the 3d and valence levels resulting from the 10 L O₂ exposure that is the first step in TPR. This correlation provides additional support for the idea that the activity-limiting factor under our conditions is the availability of adsorbed, activated oxygen. The oxidation-induced shifts are attributed to the electron withdrawing effect of forming Pd–O bonds, leaving the Pd centers with partial positive charges that increase the energy required to eject photoelectrons. Therefore, samples with larger shifts have more adsorbed oxygen, and thus their higher activity suggests that adsorbed oxygen is the limiting reactant.

Thickness Effects on Sample Electronic Band Structure. CO oxidation activity is shown to be correlated with several physical properties of the samples, including the fraction of Pd in the surface layer, the density of particular “on top” binding sites, and the Pd 3d BE shifts caused by O₂ exposure. The fact that all the core and valence levels of the alumina films shift substantially (>1 eV) in the thickness range where the dip in activity is seen (Figure 6) suggests that thickness-dependent variations in the electrostatic potential in the film may affect the physical and chemistry properties of deposited Pd₂₀. Therefore, before further addressing the thickness effects, we need to explore how thickness affects the electronic band structure of the films, using measured spectra as inputs.

The alumina films have significant surface concentrations of Re (Figure S1 of the Supporting Information), attributed to diffusion of Re from the substrate into the alumina during growth. We do not know how the Re concentration varies with depth within a particular film or the Re binding geometries (interstitial vs substitutional). As shown below, many properties of the Pd₂₀/alumina/Re samples can be rationalized in terms of a simple model, where Re atoms are assumed to be distributed within the alumina films, acting as electron donors, making the alumina an n-doped semiconductor. To model the Re depth distributions, we make the assumption that the dependence of bulk concentration on distance from the Re substrate can be equated with the dependence of the surface concentration on film thickness; i.e., we assume that the thinner films look like slices of a thick film. We have no way to measure the actual Re depth distribution, although we note that if Re ISS is monitored as the He⁺ beam is allowed to slowly sputter the surface, the Re intensity increases gradually, as would be expected from this assumption. Because the thinnest films are discontinuous, the Re surface concentration in the alumina portion of the films was estimated by extrapolating the trend observed for the thicker, continuous films, giving Re dopant concentration

estimates that range from $\sim 2 \times 10^{21}/\text{cm}^3$ close to the alumina-Re interface, dropping to $\sim 3 \times 10^{20}/\text{cm}^3$ near the surface of a thick film.

It is not unreasonable that Re should act as an electron donor, because it has a range of oxidation states, most of which are greater than the 3+ state of Al. For the purposes of illustrating how the alumina electronic properties might vary with thickness, the particular oxidation state is not important. Consider the case where each Re atom donates, on average, one electron to the alumina conduction band, so that the free electron density (N_d) is equal to the Re dopant density. The resulting N_d values ($3 \times 10^{20}/\text{cm}^3$ to $2 \times 10^{21}/\text{cm}^3$) are large compared to those in typical doped semiconductors ($< 10^{18}/\text{cm}^3$)⁹² but still substantially lower than the electron densities in metals (e.g., 8.5×10^{22} for copper).

To understand how the thickness of such a highly doped alumina film might tune the properties of supported Pd₂₀ clusters, it is important to understand electron transfer between the alumina film and the Re support and the resulting effects on the alumina electronic bands. Common band structure models for metal–metal and metal–semiconductor contacts are reviewed in the Supporting Information (Figures S4–S6). Figure 9 outlines a band structure model for contact between surface-oxidized ReO_x and a thick Re-doped alumina film. Figure 9a shows our estimate of the projected occupied density of states (pDOS) for ReO_x (left) and Re-doped alumina (right), before the two are brought into contact. The pDOS for ReO_x is simply the measured UPS for the surface-oxidized Re sample, referenced to E_F of the Re(0001) support (E_F^{Re}). As noted above, the UPS sampling depth is ~ 2 nm, and thus the pDOS plotted includes contributions both from bulk-like metallic Re and the oxidized surface. The measured work function for the ReO_x surface was used for Φ_{Re} , thereby determining E_{vac} . Before contact, the vacuum levels (E_{vac}) over each component are identical because each is electrically neutral.

Obviously, we are not able to measure the UPS for a freestanding alumina film, and the pDOS plotted for alumina is the measured UPS for a 2.8 nm thick alumina/Re sample, modified as follows: We have added a postulated impurity band of Re donor states in the alumina band gap (shaded red). The presence of states near the conduction band minimum would lead to significant density of free (conduction) electrons and also shift the Fermi level for alumina (E_F^{alumina}) close to the bottom of the conduction band. The measured work function for this thick alumina/Re sample was used for Φ_{alumina} , thereby positioning E_F^{alumina} relative to E_{vac} . The figure also indicates the electron affinity of the alumina, EA.

Figure 9b shows the situation after contact. Because the Re sample is grounded, the ReO_x energy levels should be unchanged after contact with alumina. The pDOS plotted for alumina is simply the UPS for the 2.8 nm thick alumina/Re sample, and because of the thickness of the alumina layer, the pDOS is dominated by a signal from the near-surface region of the alumina. The states in the alumina film that had precontact energies above E_F^{Re} have been depopulated by electron transfer to Re, thereby dropping E_F^{alumina} into alignment with E_F^{Re} , and positively charging the alumina layer with respect to the grounded Re sample. The positive electrical potential in the film stabilizes the electronic energy levels of the alumina film by $\Delta\chi$, consistent with the observation that the alumina BEs for alumina/Re are substantially higher than those for bulk alumina (Figure 6a).

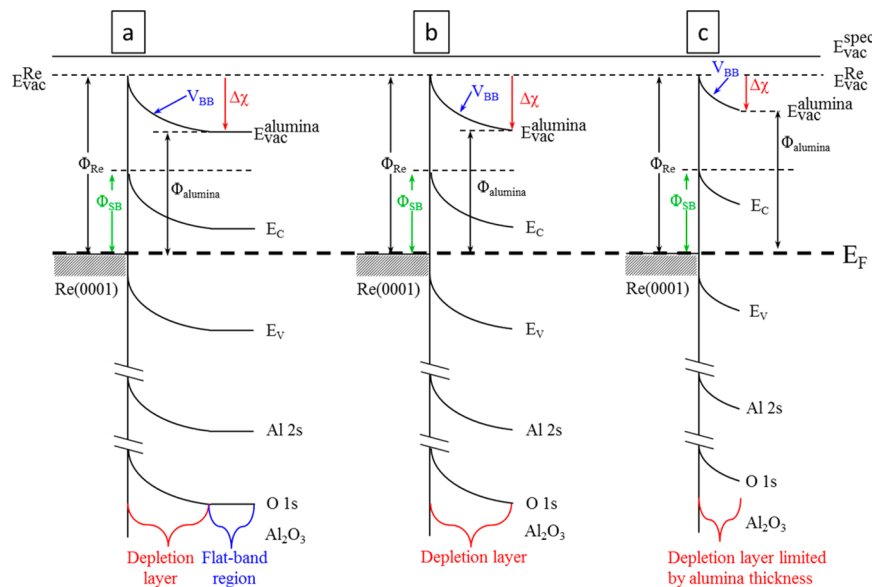


Figure 10. Potential energy diagrams illustrating band bending expected for contact of Re with alumina films of thickness (a) much greater than the depletion layer thickness, (b) comparable to the depletion layer thickness, and (c) thinner than the depletion layer.

To understand the thickness dependence of the BE shifts, we need to understand the variation in the electronic properties with distance from the Re–alumina interface. Figures S5 and S6, and accompanying discussion in the Supporting Information review the standard Schottky–Mott model^{93,94} for contact between a metal and an n-doped semiconductor. Specific examples relevant to contact between Re and highly doped alumina films of different thicknesses are shown in Figure 10. Figure 10a shows a simplified version of the band diagram for ReO_x in contact with a thick alumina film, where the horizontal position represents distance from the Re–alumina interface, which is indicated by the vertical line. As in Figure 9b, free electrons originating from the Re dopant atoms in the alumina film transfer to Re upon contact, aligning the Fermi levels of Re and alumina. Because the metal is conductive, the transferred electrons localize at the Re side of the Re–alumina interface, but the corresponding positive charge is distributed over a thin depletion layer within the alumina, where the free electron density is depleted leaving behind a corresponding density of unscreened Re cations. This charge distribution results in a positive potential building up across the depletion layer and creation of a Schottky barrier (Φ_{SB}). Within the depletion layer, the potential varies with distance from the interface, causing the electronic bands to bend, as discussed in the Supporting Information.

In the near-surface region of thick alumina films (outside the depletion layer), the electronic bands are flat and stabilized by $\Delta\chi$. As a result, the alumina core and valence BEs are shifted to higher energy and independent of alumina thickness, as long as the films are thick enough that XPS and UPS do not “see” the depletion layer. This corresponds to the situation for films thicker than ~4 nm in Figure 6a. The shift in the vacuum level implies that the work function for thick films should be low and thickness-independent, as shown in Figure 5b. The pDOS shown in Figure 9b, for the near-surface region of a thick film alumina/Re sample, corresponds to this flat-band portion of the band diagram.

The center diagram is for Re in contact with an alumina film with thickness only slightly greater than the depletion layer.

The alumina-to-Re electron transfer and the resulting alumina surface potential are still limited by the depletion layer, as in the thicker films; however, the XPS and UPS measurements now sample through the flat-band region, into the depletion layer. The effective attenuation lengths⁶⁶ for Al 2s and O 1s photoelectrons in alumina are 2.9 and 2.1 nm, respectively (for Al K α radiation); thus, the measured alumina BEs are an exponentially weighted average over the top ~5 nm of the samples. Similarly, the inelastic mean-free path for electrons with kinetic energy corresponding to the top of the alumina valence band is ~1 nm;⁹⁵ therefore, the valence band onset energy is also averaged over the top few nanometers of the samples. Therefore, with decreasing film thickness in this range, we expect the XPS and UPS spectra to become thickness-dependent, as the spectra increasingly sample the potential gradient across the depletion layer.⁹² As shown in Figure 6a, the BEs measured by XPS and UPS begin to shift to lower energies for films thinner than ~4 nm. In addition, the full width at half-maximum (fwhm) of the XPS peaks (e.g., Al 2s) increases from 2.5 eV for films thicker than ~3 nm to 3 eV for the thinnest alumina films, due to the potential gradient across the films.

The right-hand diagram shows the situation for Re in contact with an alumina film that is thinner than the depletion layer (i.e., thinner than the depletion layer would be in a thick film). In this scenario, the alumina-to-Re electron transfer is limited by the small number of free electrons in the thin alumina film. Therefore, the positive potential built up across the film is smaller than for thicker alumina, resulting in less stabilization of the alumina BEs. As shown in Figure 6a, the alumina BEs become strongly thickness-dependent for films thinner than ~1.8 nm, suggesting that the depletion layer is somewhat thinner than that (because the BEs average over the near-surface region). Also, because the vacuum level stabilization is smaller for thinner films, the work function should increase with decreasing alumina thickness, as is seen in Figure 5b. Finally, as already noted, the fwhm of the XPS peaks should be large, because of the potential gradient across the alumina film, as is observed.

In addition to the effect of thickness on alumina electronic properties, we need to account for several observations relating to Pd_{20} deposition. It is found that depositing 0.1 ML-equivalent of Pd_{20} results in significant (~ 0.4 eV) shifts of the alumina core and valence levels to lower BE for the thicker alumina/Re samples (Figure 6a); however, there is no shift for samples with alumina films thinner than ~ 1.5 nm. On the other hand, despite the fact that the core and valence levels of the alumina films shift by more than 1 eV with changing film thickness, the Pd 3d BEs for $\text{Pd}_{20}/\text{alumina}/\text{Re}$ are independent of alumina thickness, within the uncertainty (Figure 6b). Finally, it is observed that while the work function of the samples is strongly dependent on alumina thickness (Figure 5b), Pd_{20} deposition has negligible (< 0.1 eV) effect on the work function.

The electrostatic/depletion layer model can rationalize at least the first two effects. First consider Pd_{20} deposited on thick alumina, where the alumina BEs are shifted ~ 1.6 eV higher than in bulk alumina, due to charging of the alumina layer by alumina-to-Re electron transfer. If there were no electron transfer between alumina and Pd_{20} , we would expect the Pd 3d BE to be shifted > 1.6 eV above the bulk value (335.3 eV).⁹⁶ This expected shift is the sum of the ~ 1.6 eV shift from the positive surface potential of the alumina film, and an additional shift from reduced final state screening in small clusters, compared to that in bulk Pd.^{75–79,97,98} For example, Auger parameter analysis for Pd atoms deposited on SiO_2 indicates that the final state is destabilized by ~ 0.8 eV compared to bulk Pd.³⁶ The Pd 3d BEs for our samples are ~ 336 eV, which is only ~ 0.7 eV higher than the bulk value.⁹⁶ The smaller-than-expected shift suggests, therefore, that there is significant electron transfer from alumina to Pd_{20} , partially canceling the shifts expected from the alumina surface potential and final state effects. To maintain alignment of E_F^{alumina} with E_F^{Re} , this alumina-to-Pd electron transfer must be compensated by less electron transfer to Re, which would reduce the potential shift between alumina and the grounded Re substrate. This effect accounts for the observation that Pd_{20} deposition causes a ~ 0.4 eV decrease in the alumina BEs for thick films, as shown in Figure 6a.

For alumina films that are thinner than the depletion layer, there are several differences. Because the surface is electron-depleted, we expect little alumina-to-Pd electron transfer compared to Pd_{20} on thick alumina, explaining why Pd_{20} deposited on films thinner than ~ 1.5 nm does not cause shifts in the alumina levels. The lack of alumina-to-Pd electron transfer would also tend to shift the Pd 3d BEs to higher energy on the thinnest films, and the low density of free electrons at the surface of these films may cause a further shift to higher BE due to reduced screening of the final state of the supported Pd. On the other hand, the amount of alumina-to-Re electron transfer also decreases for the thinnest films, resulting in less positive alumina surface potentials, which tends to decrease the Pd 3d BEs. Evidently, the three effects largely cancel, such that the Pd BEs are thickness-independent within ~ 0.2 eV.

The one measurement that appears inconsistent with the idea that there is alumina-to-Pd electron transfer upon Pd_{20} deposition on the thicker films is the observation that the sample work function does not change significantly upon Pd_{20} deposition. If Pd_{20} accepts electrons from alumina, we might expect that the corresponding surface dipole layer should result in a Pd_{20} -induced increase in work function. We have no explanation for this lack of effect; however, we note that a

number of groups have reported detailed studies of the effects of anionic adsorbates on work functions, showing that even in cases where a negative surface dipole forms, there is not necessarily an increase in work function.^{99–101}

Thickness Effects, Pd_{20} Binding Geometry, and Correlations with Activity. As shown in Figure 8, the Pt ISS intensity varies with alumina thickness in a way that correlates with CO oxidation activity, the density of high temperature CO binding sites (Figure 4), and the tendency of the Pd_{20} to oxidize during O_2 exposure (Figure 7). The ISS result indicates that the number of Pd atoms in the surface layer goes through a $\sim 14\%$ dip as the alumina thickness varies between 1 and 3 nm. It is, therefore, not surprising that the density of CO binding sites also dips, given the indication from TD-ISS studies⁶² that the high temperature CO is bound on top of the Pd clusters. Similarly, we might expect a dip in activity as well, because CO oxidation appears to require Pd sites. It is interesting, however, that the dips for high temperature CO binding ($\sim 25\%$) and CO oxidation activity ($\sim 50\%$) are considerably larger than the dip in Pd surface availability.

Before addressing the correlation between these observables, it is useful to discuss what changes in sample morphology might be responsible for the $\sim 14\%$ variation in Pd ISS intensity. One possibility is that Pd_{20} deposited on alumina in the 1 to 3 nm range is prone to sintering at room temperature, producing larger particles with a smaller fraction of Pd in the surface layer, and thus reducing the as-deposited Pd ISS intensity. If sintering were significant for $\text{Pd}_{20}/\text{alumina}$ at room temperature, it should be greatly accelerated by heating to 560 K during the TPR/TPD runs, and we would expect to see evolution in the CO and CO_2 desorption behavior during the sequence of three TPR experiments. Sintering during TPR and TPD runs would also result in postreaction Pd ISS intensity that is substantially lower than the as-deposited intensity. As discussed above, there is little evolution in the TPR signals and no evidence of sintering in the postreaction ISS, implying that sintering at temperatures up to 560 K is not facile.

Instead, we attribute the thickness-dependent dip in Pd ISS intensity to changes in the as-deposited cluster morphology. A study of cluster size effects on ISS suggests that Pd_{20} deposits as flattened islands on thick alumina films, with all but a few Pd atoms in the surface layer.⁶² The 14% dip in Pd ISS intensity would simply require that the Pd_{20} adopted slightly more compact, multilayer geometries. Given the changes in alumina surface potential, work function, and band structure that occur in the 1 to 3 nm thickness range, it would not be surprising if the Pd–alumina bond strength also changed, leading to thickness-dependent morphology.

Origin of the Thickness-Dependent Activity Dip. One goal of investigating the effects of alumina thickness on activity is to use thickness-dependent correlations of activity with other properties of the samples (Figures 4 and 6–8) to gain insight into the reaction mechanism and factors that control activity. Taken together, the changes in various physical properties with alumina thickness suggest the following explanation for the thickness dependence of the CO oxidation activity: Because only samples with Pd_{20} are active and activated oxygen is the limiting reactant, it is clear that O_2 binding and activation to Pd_{20} is the critical step under our TPR conditions. O_2 activation typically involves electron transfer from the catalytic center to the antibonding π^* orbital of O_2 , weakening the O_2 bond. Therefore, we might expect activity to be enhanced for clusters

in electron-rich environments. In addition, the correlation of activity with the density of “on-top” binding sites suggests that oxygen activation also requires sites on top of the Pd₂₀.

As discussed above, for Pd₂₀ deposited on alumina films that are much thicker than the depletion layer, the alumina surface layer has free electrons available, and the XPS/UPS evidence indicates that there is significant electron transfer from alumina to Pd₂₀. At the same time, the ISS results suggest that the Pd₂₀ structure exposes a large fraction of the Pd in the surface layer, which is consistent with the observation from TPD, that Pd₂₀ on thick alumina exposes a high density of “on-top” binding sites. The combination of electron rich clusters with a high density of the sites required for oxygen activation leads to high CO oxidation activity, which is thickness-independent as long as the film is much thicker than the depletion layer.

For samples with thinner alumina films, the alumina layer is depleted of electrons. This should reduce (or eliminate) electron transfer to Pd₂₀, which, in turn, should reduce the ability of Pd₂₀ to activate and bind O₂ by electron transfer into the π^* orbital. Furthermore, the decreases in Pd ISS intensity for these samples suggest that the clusters have more three-dimensional morphology than for thicker alumina, which one might expect as another consequence of electron depletion at the alumina surface. The morphology change is consistent with the lower density of “on-top” binding sites observed by CO TPD. The 50% reduction in activity is, therefore, attributed to the combination of lower electron density in the supported Pd₂₀ and changes in Pd₂₀ morphology.

In this system, activity is also relatively high for Pd₂₀ deposited directly on the oxidized ReO_x surface. The fact that the work function for ReO_x (7.3 eV) is substantially higher than that of the Re(0001) (Figure 5b) suggests that there is a negative surface dipole, consistent with termination by an electron-rich oxygen layer. It is not unreasonable to suppose that Pd₂₀ deposited on such an electron-rich surface layer would bind strongly and undergo significant ReO_x-to-Pd electron transfer, as suggested by the observation that the Pd 3d BE for Pd₂₀/ReO_x is significantly lower than for Pd₂₀ on any of the alumina films (Figure 6b). Strong Pd-ReO_x binding is consistent with these clusters having flattened structures (high Pd ISS intensity), which in turn, provide a high density of “on-top” binding sites (intense high temperature CO desorption). The combination of electron-rich clusters with a high density of binding sites for O₂ activation is presumably responsible for the high activity of the Pd₂₀/ReO_x samples.

5. CONCLUSIONS

We have exploited the ability to deposit size-selected cluster ions to prepare a series of samples with identical coverage of Pd₂₀ clusters, but with variable thickness alumina films. XPS and UPS show that electrons transfer from the alumina films to Re, creating a depletion layer in the alumina 1 to 1.5 nm thick. The CO oxidation activity is low for Pd₂₀ deposited alumina films with thicknesses similar to or thinner than the depletion layer, because such films provide an electron-poor environment, which affects both O₂ activation and the geometry of the deposited Pd₂₀. For thicker alumina layers, the Pd₂₀ becomes electron rich due to electron transfer from the alumina film, enhancing O₂ activation and CO oxidation activity. The alumina–Pd binding is also stronger on the thicker films, resulting in flatter cluster structures that provide more binding sites for both O₂ and CO adsorption.

■ ASSOCIATED CONTENT

S Supporting Information

Detailed explanation of the estimation of Re doping density in the alumina films (Figure S1), fitting process used to separate the low and high temperature CO desorption peaks (Figure S2), identification of the Pd valence band onset (Figure S3), and a review of Schottky barriers and the electron transfer process resulting from dissimilar materials placed in contact (Figures S4–S7). This material is available free of charge via the Internet at <http://pubs.acs.org>.

■ AUTHOR INFORMATION

Corresponding Author

*E-mail: anderson@chem.utah.edu. Fax: +801 5816681. Tel.: +801 585 7289.

Notes

The authors declare no competing financial interest.

■ ACKNOWLEDGMENTS

This work was funded by a Basic Research Initiative grant from the Air Force Office of Scientific Research (AFOSR FA9550-12-1-0481). We gratefully acknowledge helpful discussions from Professor Clayton Williams (University of Utah, Physics)

■ REFERENCES

- (1) Zhang, J.; Alexandrova, A. N. The Golden Crown: A Single Au Atom that Boosts the CO Oxidation Catalyzed by a Palladium Cluster on Titania Surfaces. *J. Phys. Chem. Lett.* **2013**, *4*, 2250–2255.
- (2) Beniya, A.; Isomura, N.; Hirata, H.; Watanabe, Y. Lateral Displacement in Soft-Landing Process and Electronic Properties of Size-Selected Pt7 Clusters on the Aluminum Oxide Film on NiAl(110). *Chem. Phys. Lett.* **2013**, *576*, 49–54.
- (3) Zhou, J.; Zhou, J.; Camillone, N., III; White, M. G. Electronic Charging of Non-Metallic Clusters. Size-Selected Mo₃y Clusters Supported on an Ultrathin Alumina Film on NiAl(110). *Phys. Chem. Chem. Phys.* **2012**, *14*, 8105–8110.
- (4) Robles, R.; Khanna, S. N. Oxidation of Pdn ($n=1–7, 10$) Clusters Supported on Alumina/NiAl(110). *Phys. Rev. B: Condens. Matter Mater. Phys.* **2010**, *82*, 085428/1–085428/6.
- (5) Maurice, V.; Fremy, N.; Marcus, P. Hydroxylation-Induced Modifications of the Al₂O₃/NiAl(001) Surface at Low Water Vapor Pressure. *Surf. Sci.* **2005**, *581*, 88–104.
- (6) Fan, C.; Wu, T.; Kaden, W. E.; Anderson, S. L. Cluster Size Effects on Hydrazine Decomposition on Irn/Al₂O₃/NiAl(110). *Surf. Sci.* **2006**, *600*, 461–467.
- (7) Vaida, M. E.; Bernhardt, T. M.; Barth, C.; Esch, F.; Heiz, U.; Landman, U. Ultrathin Magnesia Films as Support for Molecules and Metal Clusters: Tuning Reactivity by Thickness and composition. *Phys. Status Solidi B* **2010**, *247*, 1001–1015.
- (8) Abbott, H. L.; Aumer, A.; Lei, Y.; Asokan, C.; Meyer, R. J.; Sterrer, M.; Shaikhutdinov, S.; Freund, H.-J. CO Adsorption on Monometallic and Bimetallic Au–Pd Nanoparticles Supported on Oxide Thin Films. *J. Phys. Chem. C* **2010**, *114*, 17099–17104.
- (9) Yoon, B.; Landman, U.; Habibpour, V.; Harding, C.; Kunz, S.; Heiz, U.; Moseler, M.; Walter, M. Oxidation of Magnesia-Supported Pd₃₀ Nanoclusters and Catalyzed CO Combustion: Size-Selected Experiments and First-Principles Theory. *J. Phys. Chem. C* **2012**, *116*, 9594–9607.
- (10) Goodman, D. W. Chemical and Spectroscopic Studies of Metal Oxide Surfaces. *J. Vac. Sci. Technol., A* **1996**, *14*, 1526–1531.
- (11) Freund, H. J.; Baumer, M.; Kuhlenbeck, H. Catalysis and Surface Science: What do We Learn from Studies of Oxide-Supported Cluster Model Systems? *Adv. Catal.* **2000**, *45*, 333–384.
- (12) Freund, H. J.; Pacchioni, G. Oxide Ultra-Thin Films on Metals: New Materials for the Design of Supported Metal Catalysts. *Chem. Soc. Rev.* **2008**, *37*, 2224–2242.

- (13) Gao, F.; Goodman, D. W. Model Catalysts: Simulating the Complexities of Heterogeneous Catalysts. *Annu. Rev. Phys. Chem.* **2012**, *63*, 265–286.
- (14) Goodman, D. W. Model Catalysts: from Extended Single Crystals to Supported Particles. *Surf. Rev. Lett.* **1995**, *2*, 9–24.
- (15) Street, S. C.; Goodman, D. W. Chemical and Spectroscopic Studies of Ultrathin Oxide Films. *Chem. Phys. Solid Surf.* **1997**, *8*, 375–406.
- (16) Campbell, C. T. Ultrathin Metal Films and Particles on Oxide Surfaces: Structural, Electronic and Chemisorptive Properties. *Surf. Sci. Rep.* **1997**, *27*, 1–112.
- (17) Campbell, C. T.; Grant, A. W.; Starr, D. E.; Parker, S. C.; Bondzie, V. A. Model Oxide-Supported Metal Catalysts: Energetics, Particle Thicknesses, Chemisorption and Catalytic Properties. *Top. Catal.* **2001**, *14*, 43–51.
- (18) Judai, K.; Abbet, S.; Woerz, A. S.; Heiz, U.; Henry, C. R. Low-Temperature Cluster Catalysis. *J. Am. Chem. Soc.* **2004**, *126*, 2732–2737.
- (19) Libuda, J.; Meusel, I.; Hoffmann, J.; Piccolo, L.; Henry, C. R.; Freund, H.-J. The CO Oxidation Kinetics on Supported Pd Model Catalysts: A Molecular Beam/in situ Time-Resolved Intrared Reflection Absorption Spectroscopy Study. *J. Chem. Phys.* **2001**, *114*, 4669–84.
- (20) Roettgen, M. A.; Abbet, S.; Judai, K.; Antonietti, J.-M.; Woerz, A. S.; Arenz, M.; Henry, C. R.; Heiz, U. Cluster Chemistry: Size-Dependent Reactivity Induced by Reverse Spill-Over. *J. Am. Chem. Soc.* **2007**, *129*, 9635–9639.
- (21) Lewis, K. B.; Oyama, S. T.; Somorjai, G. A. The Preparation and Reactivity of Thin, Ordered Films of Vanadium Oxide on Au(111). *Surf. Sci.* **1990**, *233*, 75–83.
- (22) Calloni, A.; Ferrari, A.; Brambilla, A.; Ciccarelli, F.; Duo, L. Growth of Stoichiometric TiO₂ Thin Films on Au(100) Substrates by Molecular Beam Epitaxy. *Thin Solid Films* **2012**, *520*, 3922–3926.
- (23) Yang, B.; Lin, X.; Gao, H.-J.; Nilius, N.; Freund, H.-J. CO Adsorption on Thin MgO Films and Single Au Adatoms: A Scanning Tunneling Microscopy Study. *J. Phys. Chem. C* **2010**, *114*, 8997–9001.
- (24) Diebold, U.; Li, S. C.; Schmid, M. Oxide Surface Science. *Annu. Rev. Phys. Chem.* **2010**, *61*, 129–148.
- (25) Nilius, N. Properties of Oxide Thin Films and their Adsorption Behavior Studied by Scanning Tunneling Microscopy and Conductance Spectroscopy. *Surf. Sci. Rep.* **2009**, *64*, 595–659.
- (26) Kresse, G.; Schmid, M.; Napetschnig, E.; Shishkin, M.; Koehler, L.; Varga, P. Structure of the Ultrathin Aluminum Oxide Film on NiAl(110). *Science (Washington, DC, U. S.)* **2005**, *308*, 1440–1442.
- (27) McCavish, N. D.; Bennett, R. A. Ultra-Thin Film Growth of Titanium Dioxide on W(100). *Surf. Sci.* **2003**, *546*, 47–56.
- (28) Murata, Y.; Nagata, K.; Fujimoto, H.; Sakurai, T.; Okada, M.; Ebe, Y. Electronic Property of Thin Single-Crystal Films of α -Al₂O₃ on Ru(0001). *J. Phys. Soc. Jpn.* **2001**, *70*, 793–796.
- (29) Sterrer, M.; Risso, T.; Heyde, M.; Rust, H.-P.; Freund, H.-J. Crossover from Three-Dimensional to Two-Dimensional Geometries of Au Nanostructures on Thin MgO(001) Films: A Confirmation of Theoretical Predictions. *Phys. Rev. Lett.* **2007**, *98*.
- (30) Wu, Y.; Garfunkel, E.; Madey, T. E. Growth of Ultrathin Crystalline Al₂O₃ Films on Ru(0001) and Re(0001) Surfaces. *J. Vac. Sci. Technol., A* **1996**, *14*, 2554–2563.
- (31) Wu, Y.; Garfunkel, E.; Madey, T. E. Growth and Oxidation of Ultra-Thin Al Films on the Re(0001) Surface. *Surf. Sci.* **1996**, *365*, 337–352.
- (32) Giordano, L.; Pacchioni, G. Oxide Films at the Nanoscale: New Structures, New Functions, and New Materials. *Acc. Chem. Res.* **2011**, *44*, 1244–1252.
- (33) Cui, Y.; Huang, K.; Nilius, N.; Freund, H.-J. Charge Competition with Oxygen Molecules Determines Growth of Gold Nanoparticles on CaO Films. *Faraday Discuss.* **2013**, *162*, 153–163.
- (34) Farmer, J. A.; Baricuatro, J. H.; Campbell, C. T. Ag Adsorption on Reduced CeO₂(111) Thin Films. *J. Phys. Chem. C* **2010**, *114*, 17166–17172.
- (35) Pacchioni, G. Electronic Interactions and Charge Transfers of Metal Atoms and Clusters on Oxide Surfaces. *Phys. Chem. Chem. Phys.* **2013**, *15*, 1737–1757.
- (36) Kaden, W. E.; Büchner, C.; Lichtenstein, L.; Stuckenholz, S.; Ringleb, F.; Heyde, M.; Sterrer, M.; Freund, H.-J.; Giordano, L.; Pacchioni, G. Understanding Surface Core-Level Shifts using the Auger Parameter; a Study of Pd Atoms Adsorbed on SiO₂ Ultra-Thin Films. *Phys. Rev. B* **2014**, *89*, 115436.
- (37) Giordano, L.; Pacchioni, G.; Noguera, C.; Goniakowski, J. Spectroscopic Evidences of Charge Transfer Phenomena and Stabilization of Unusual Phases at Iron Oxide Monolayers Grown on Pt(111). *Top. Catal.* **2013**, *56*, 1074–1081.
- (38) Jaeger, R. M.; Kuhlenbeck, H.; Freund, H.-J.; Wuttig, M.; Hoffmann, W.; Franchy, R.; Ibach, H. Formation of a Well-Ordered Aluminium Oxide Overlayer by Oxidation of NiAl. *Surf. Sci.* **1991**, *259*, 235–252.
- (39) Libuda, J.; Winkelmann, F.; Bäumer, M.; Freund, H.-J.; Bertrams, T.; Neddermeyer, H.; Müller, K. Structure and Defects of an Ordered Alumina Film on NiAl(110). *Surf. Sci.* **1994**, *318*, 61–73.
- (40) Ceballos, G.; Song, Z.; Pascual, J. I.; Rust, H.-P.; Conrad, H.; Bäumer, M.; Freund, H.-J. Structure Investigation of the Topmost Layer of a Thin Ordered Alumina Film Grown on NiAl(1 1 0) by Low Temperature Scanning Tunneling Microscopy. *Chem. Phys. Lett.* **2002**, *359*, 41–47.
- (41) Lay, T. T.; Yoshitake, M.; Mebarki, B. Temperature Effect on Growth of Well-Ordered Thin Al₂O₃ Film on NiAl(110). *J. Vac. Sci. Technol., A* **2002**, *20*, 2027–2031.
- (42) Stierle, A.; Renner, F.; Streitel, R.; Dosch, H.; Drube, W.; Cowie, B. C. X-ray Diffraction Study of the Ultrathin Al₂O₃ Layer on NiAl(110). *Science* **2004**, *303*, 1652–1656.
- (43) Shaikhutdinov, S.; Heemeier, M.; Hoffmann, J.; Meusel, I.; Richter, B.; Bäumer, M.; Kuhlenbeck, H.; Libuda, J.; Freund, H.-J.; Oldman, R.; et al. Interaction of Oxygen with Palladium Deposited on a Thin Alumina Film. *Surf. Sci.* **2002**, *501*, 270–281.
- (44) Wu, T.; Kaden, W. E.; Kunkel, W. A.; Anderson, S. L. Size-Dependent Oxidation of Pd_n ($n \leq 13$) on Alumina/NiAl(110): Correlation with Pd Core Level Binding Energies. *Surf. Sci.* **2009**, *603*, 2764–2770.
- (45) Lai, X.; Chusuei, C. C.; Luo, K.; Guo, Q.; Goodman, D. W. Imaging Ultrathin Al₂O₃ Films with Scanning Tunneling Microscopy. *Chem. Phys. Lett.* **2000**, *330*, 226–230.
- (46) Chen, P. J.; Goodman, D. W. Epitaxial Growth of Ultrathin Al₂O₃ Films on Ta(110). *Surf. Sci.* **1994**, *312*, L767–L773.
- (47) Parker, D. H.; Koel, B. E. Chemisorption of High Coverages of Atomic Oxygen on the Pt(111), Pd(111), and Au(111) Surfaces. *J. Vac. Sci. Technol., A* **1990**, *8*, 2585–2590.
- (48) Santra, A. K.; Goodman, D. W. Catalytic Oxidation of CO by Platinum Group Metals: From Ultrahigh vacuum to Elevated Pressures. *Electrochim. Acta* **2002**, *47*, 3595–3609.
- (49) Engel, T.; Ertl, G. A Molecular Beam Investigation of the Catalytic Oxidation of Carbon Monoxide on Palladium (111). *J. Chem. Phys.* **1978**, *69*, 1267–1281.
- (50) Engel, T.; Ertl, G. Surface Residence Times and Reaction Mechanism in the Catalytic Oxidation of Carbon Monoxide on Palladium(111). *Chem. Phys. Lett.* **1978**, *54*, 95–98.
- (51) Tomita, A.; Shimizu, K.-i.; Kato, K.; Akita, T.; Tai, Y. Mechanism of Low-Temperature CO Oxidation on Pt/Fe-Containing Alumina Catalysts Pretreated with Water. *J. Phys. Chem. C* **2013**, *117*, 1268–1277.
- (52) Moses-DeBusk, M.; Yoon, M.; Allard, L. F.; Mullins, D. R.; Wu, Z.; Yang, X.; Veith, G.; Stocks, G. M.; Narula, C. K. CO Oxidation on Supported Single Pt Atoms: Experimental and ab Initio Density Functional Studies of CO Interaction with Pt Atom on θ -Al₂O₃(010) Surface. *J. Am. Chem. Soc.* **2013**, *135*, 12634–12645.
- (53) Corma, A.; Concepción, P.; Boronat, M.; Sabater, M. J.; Navas, J.; Yacaman, M. J.; Larios, E.; Posadas, A.; López-Quintela, M. A.; Buceta, D.; et al. Exceptional Oxidation Activity with Size-Controlled Supported Gold Clusters of Low Atomicity. *Nat. Chem.* **2013**, *5*, 775–781.

- (54) Brandt, B.; Schalow, T.; Laurin, M.; Schauermann, S.; Libuda, J.; Freund, H.-J. Oxidation, Reduction, and Reactivity of Supported Pd Nanoparticles: Mechanism and Microkinetics. *J. Phys. Chem. C* **2007**, *111*, 938–949.
- (55) Tang, X.; Schneider, J.; Dollinger, A.; Luo, Y.; Woerz, A. S.; Judai, K.; Abbet, S.; Kim, Y. D.; Gantefoer, G. F.; Fairbrother, D. H.; et al. Very Small “Window of Opportunity” for Generating CO Oxidation-Active Au_n on TiO₂. *Phys. Chem. Chem. Phys.* **2014**, *16*, 6735–6742.
- (56) Bondzie, V. A.; Parker, S. C.; Campbell, C. T. The Kinetics of CO Oxidation by Adsorbed Oxygen on Well-Defined Gold Particles on TiO₂(110). *Catal. Lett.* **1999**, *63*, 143–151.
- (57) Bourane, A.; Bianchi, D. Oxidation of CO on a Pt/Al₂O₃ Catalyst: from the surface Elementary Steps to Light-Off Tests IV. Kinetic Study of the Reduction by CO of Strongly Adsorbed Oxygen Species. *J. Catal.* **2003**, *220*, 3–12.
- (58) Conrad, H.; Ertl, G.; Kueppers, J. Interactions Between Oxygen and Carbon Monoxide on a Palladium (111) Surface. *Surf. Sci.* **1978**, *76*, 323–342.
- (59) McClure, S. M.; Goodman, D. W. New Insights into Catalytic CO Oxidation on Pt-Group Metals at Elevated Pressures. *Chem. Phys. Lett.* **2009**, *469*, 1–13.
- (60) Winans, R. E.; Vajda, S.; Ballantine, G. E.; Elam, J. W.; Lee, B.; Pellin, M. J.; Seifert, S.; Tikhonov, G. Y.; Tomczyk, N. A. Reactivity of Supported Platinum Nanoclusters Studied by *in situ* GISAXS: Clusters Stability under Hydrogen. *Top. Catal.* **2006**, *39*, 145–149.
- (61) Kane, M. D.; Roberts, F. S.; Anderson, S. L. Alumina Support and Pd_n Cluster Size Effects on Activity of Pd_n for Catalytic Oxidation of CO. *Faraday Discuss.* **2013**, *162*, 323–340.
- (62) Kane, M. D.; Roberts, F. S.; Anderson, S. L. Mass-Selected Supported Cluster Catalysts: Size Effects on CO Oxidation Activity, Electronic Structure, and Thermal Stability of Pd_n/alumina ($n \leq 30$) Model Catalysts. *Int. J. Mass Spectrom.* **2014**, *370*, 1–15.
- (63) Aizawa, M.; Lee, S.; Anderson, S. L. Sintering, Oxidation, and Chemical Properties of Size-Selected Nickel Clusters on TiO₂ (110). *J. Chem. Phys.* **2002**, *117*, 5001–5011.
- (64) Kaden, W. E.; Kunkel, W. A.; Roberts, F. S.; Kane, M.; Anderson, S. L. CO Adsorption and Desorption on Size-Selected Pdn/TiO₂(110) Model Catalysts: Size Dependence of Binding Sites and Energies, and Support-Mediated Adsorption. *J. Chem. Phys.* **2012**, *136*, 204705/1–204705/12.
- (65) Yeh, J. J.; Lindau, I. Atomic Subshell Photoionization Cross Sections and Asymmetry Parameters: $1 < Z < 103$. *At. Data Nucl. Data Tables* **1985**, *32*, 1–155.
- (66) Powell, C. J.; Jablonski, A. *NIST Electron Effective-Attenuation-Length Database*, version 1.3; NIST: Gaithersburg, MD, 2011.
- (67) Lee, S.; Fan, C.; Wu, T.; Anderson, S. L. Hydrazine Decomposition over Ir_n/Al₂O₃ Model Catalysts Prepared by Size-Selected Cluster Deposition. *J. Phys. Chem. B* **2005**, *109*, 381–388.
- (68) Kaden, W. E.; Kunkel, W. A.; Roberts, F. S.; Kane, M.; Anderson, S. L. Thermal and Adsorbate Effects on the Activity and Morphology of Size-Selected Pdn/TiO₂ Model Catalysts. *Surf. Sci.* **2014**, *621*, 40–50.
- (69) Rabalais, J. W. *Principles and applications of ion scattering spectrometry: surface chemical and structural analysis*; Wiley: New York, 2003; p 336.
- (70) Aizawa, M.; Lee, S.; Anderson, S. L. Deposition Dynamics and Chemical Properties of Size-Selected Ir Clusters on TiO₂. *Surf. Sci.* **2003**, *542*, 253–275.
- (71) Kaden, W. E.; Kunkel, W. A.; Anderson, S. L. Cluster Size Effects on Sintering, CO Adsorption, and Implantation in Ir/SiO₂. *J. Chem. Phys.* **2009**, *131*, 114701-1–114701-15.
- (72) Englemann, A. Über die Bestimmung der Lichtelektrischen Grenzwellenlänge am Rhenium. *Ann. Phys.* **1933**, *409*, 185–208.
- (73) Schlaf, R.; Schroeder, P. G.; Nelson, M. W.; Parkinson, B. A.; Merritt, C. D.; Crisafulli, L. A.; Murata, H.; Kafafi, Z. H. Determination of Interface Dipole and Band Bending at the Ag/tris (8-hydroxyquinolinato) Gallium Organic Schottky Contact by Ultraviolet Photoemission Spectroscopy. *Surf. Sci.* **2000**, *450*, 142–152.
- (74) Levy, R.; Boudart, M. Platinum-like Behavior of Tungsten Carbide in Surface Catalysis. *Science* **1973**, *181*, 547–549.
- (75) K itsudo, Y.; Iwamoto, A.; Matsumoto, H.; Mitsuhara, K.; Nishimura, T.; Takizawa, M.; Akita, T.; Maeda, Y.; Kido, Y. Final State Effect for Au 4f line from Gold-Nano-Particles Grown on Oxides and HOPG Supports. *Surf. Sci.* **2009**, *603*, 2108–2114.
- (76) Tao, J. G.; Pan, J. S.; Huan, C. H. A.; Zhang, Z.; Chai, J. W.; Wang, S. J. Origin of XPS Binding Energy Shifts in Ni Clusters and Atoms on Rutile TiO₂ Surfaces. *Surf. Sci.* **2008**, *602*, 2769–2773.
- (77) Bellamy, B.; Mechken, S.; Masson, A. Metallic Clusters Surface Interaction: the Case of Palladium/Silicon Oxide (SiO_x)/n-Silicon (100). *Z. Phys. D: At., Mol. Clusters* **1993**, *26*, 61–63.
- (78) Wertheim, G. K. Electronic Structure of Metal Clusters. *Z. Phys. D: At., Mol. Clusters* **1989**, *12*, 319–326.
- (79) Mason, M. G. Electronic Structure of Supported Small Metal Clusters. *Phys. Rev. B* **1983**, *27*, 748–62.
- (80) Langmuir, I. The Mechanism of the Catalytic Action of Platinum in the Reactions $2\text{CO} + \text{O}_2 \rightarrow 2\text{CO}_2$ and $2\text{H}_2 + \text{O}_2 \rightarrow 2\text{H}_2\text{O}$. *Trans. Faraday Soc.* **1922**, *17*, 621–654.
- (81) Langmuir, I. Chemical Reactions on Surfaces. *Trans. Faraday Soc.* **1921**, *17*, 607–620.
- (82) Libuda, J.; Meusel, I.; Hoffmann, J.; Hartmann, J.; Freund, H.-J. Reaction Kinetics on Supported Model Catalysts: Molecular Beam/*in situ* Time-Resolved Infrared Reflection Absorption Spectroscopy Study of the CO Oxidation on Alumina Supported Pd Particles. *J. Vac. Sci. Technol. A* **2001**, *19*, 1516–1523.
- (83) Meusel, I.; Hoffmann, J.; Hartmann, J.; Heemeier, M.; Bäumer, M.; Libuda, J.; Freund, H.-J. The Interaction of Oxygen with Alumina-Supported Palladium Particles. *Catal. Lett.* **2001**, *71*, 5–13.
- (84) Meusel, I.; Hoffmann, J.; Hartmann, J.; Libuda, J.; Freund, H.-J. Size Dependent Reaction Kinetics on Supported Model Catalysts: A Molecular Beam/IRAS Study of the CO Oxidation on Alumina-Supported Pd Particles. *J. Phys. Chem. B* **2001**, *105*, 3567–3576.
- (85) Stara, I.; Matolin, V. The Influence of Particle Size on CO Adsorption on Pd/alumina Model Catalysts. *Surf. Sci.* **1994**, *313*, 99–106.
- (86) Gillet, E.; El-Yakhloifi, M. H. Supported Palladium (Pdn) ($n=1–20$) Cluster Reactivity: Carbon Monoxide Chemisorption. *Z. Phys. D: At., Mol. Clusters* **1993**, *26*, 64–66.
- (87) Chen, M. S.; Cai, Y.; Yan, Z.; Gath, K. K.; Axnanda, S.; Goodman, D. W. Highly Active Surfaces for CO Oxidation on Rh, Pd, and Pt. *Surf. Sci.* **2007**, *601*, 5326–5331.
- (88) Kaden, W. E.; Kunkel, W. A.; Kane, M. D.; Roberts, F. S.; Anderson, S. L. Size-Dependent Oxygen Activation Efficiency over Pdn/TiO₂(110) for the CO Oxidation Reaction. *J. Am. Chem. Soc.* **2010**, *132*, 13097–13099.
- (89) Jones, I. Z.; Bennett, R. A.; Bowker, M. CO Oxidation on Pd(110): a High-Resolution XPS and Molecular Beam Study. *Surf. Sci.* **1999**, *439*, 235–248.
- (90) Roberts, F. S.; Kane, M. D.; Baxter, E. T.; Anderson, S. L. Oxygen Activation and CO Oxidation over Size-Selected Ptn/alumina/Re(0001) Model Catalysts: Correlations with Valence Electronic Structure, Physical Structure, and Binding Sites. *Phys. Chem. Chem. Phys.* **2014**, *16*, 26443–26457.
- (91) Proch, S.; Wirth, M.; White, H. S.; Anderson, S. L. Strong Effects of Cluster Size and Air Exposure on Oxygen Reduction and Carbon Oxidation Electrocatalysis by Size-Selected Pt_n ($n \leq 11$) on Glassy Carbon Electrodes. *J. Am. Chem. Soc.* **2013**, *135*, 3073–3086.
- (92) Zhang, Z.; Yates, J. T., Jr. Band Bending in Semiconductors: Chemical and Physical Consequences at Surfaces and Interfaces. *Chem. Rev.* **2012**, *112*, 5520–5551.
- (93) Schottky, W. The Semiconductor Theory of the Blocking Layer and Point Rectifier. *Z. Phys.* **1939**, *113*, 367–414.
- (94) Mott, N. F. The Contact Between a Metal and an Insulator or Semiconductor. *Proc. Cambridge Philos. Soc.* **1938**, *34*, 568–572.
- (95) Somorjai, G. A. *Chemistry in Two Dimensions: Surfaces*; Cornell University Press: Ithaca, NY, 1981.

- (96) Moulder, J. F.; Stickle, W. F.; Sobol, P. E.; Bomben, K. D.; Chastain, J.; King, R. C., Jr., eds, *Handbook of X-ray Photoelectron Spectroscopy*; Physical Electronics: Eden Prarie, MN, 1995.
- (97) Peters, S.; Peredkov, S.; Neeb, M.; Eberhardt, W.; Al-Hada, M. Size-Dependent XPS Spectra of Small Supported Au-Clusters. *Surf. Sci.* **2013**, *608*, 129–134.
- (98) Mao, B.-H.; Chang, R.; Lee, S.; Axnanda, S.; Crumlin, E.; Grass, M. E.; Wang, S.-D.; Vajda, S.; Liu, Z. Oxidation and Reduction of Size-Selected Subnanometer Pd Clusters on Al₂O₃ Surface. *J. Chem. Phys.* **2013**, *138*, 214304–214311.
- (99) Michaelides, A.; Hu, P.; Lee, M. H.; Alavi, A.; King, D. *Phys. Rev. Lett.* **2003**, *90*, 246103.
- (100) Bagus, P.; Käfer, D.; Witte, G.; Wöll, C. Work Function Changes Induced by Charged Adsorbates: Origin of the Polarity Asymmetry. *Phys. Rev. Lett.* **2008**, *100*, 125501.
- (101) Leung, T.; Kao, C.; Su, W.; Feng, Y.; Chan, C. Relationship Between Surface Dipole, Work Function and Charge Transfer: Some Exceptions to an Established Rule. *Phys. Rev. B* **2003**, *68*, 195408.